Application of a Satellite-Retrieved Sheltering Parameterization (v1.0) for Dust Event Simulation with WRF-Chem v4.1

Sandra L. LeGrand[1,2], Theodore W. Letcher[3], Gregory S. Okin[2], Nicholas P. Webb[4], Alex R. Gallagher[3], Saroj Dhital[4], Taylor S. Hodgdon[3], Nancy P. Ziegler[3], and Michelle L. Michaels[3]

[1]U.S. Army Engineer Research and Development Center, Geospatial Research Laboratory, Alexandria, Virginia, USA
[2]Department of Geography, University of California, Los Angeles, California, USA
[3]U.S. Army Engineer Research and Development Center, Cold Regions Research and Engineering Laboratory, Hanover, New Hampshire, USA
[4]USDA-ARS Jornada Experimental Range, Las Cruces, New Mexico, USA

Correspondence: Sandra LeGrand (Sandra.L.LeGrand@usace.army.mil)

Abstract. Roughness features (e.g., rocks, vegetation, furrows, etc.) that shelter or attenuate wind flow over the soil surface can considerably affect the magnitude and spatial distribution of sediment transport in active aeolian environments. Existing dust and sediment transport models often rely on vegetation attributes derived from static land-use datasets or remotely-sensed greenness indicators to incorporate sheltering effects on simulated particle mobilization. However, these overly simplistic approaches do not represent the three-dimensional nature or spatiotemporal changes of roughness element sheltering. They also ignore the sheltering contribution of non-vegetation roughness features and photosynthetically-inactive (i.e., brown) vegetation common to dryland environments. Here, we explore the use of a novel albedo-based sheltering parameterization in a dust transport modeling application of the Weather Research and Forecasting model with Chemistry (WRF-Chem). The albedo method estimates sheltering effects on surface wind friction speeds and dust entrainment from the shadows cast by subgrid-scale roughness elements. For this study, we applied the albedo-derived drag partition to the Air Force Weather Agency (AFWA) dust emission module and conducted a sensitivity study on simulated PM_{10} concentrations using the Georgia Institute of Technology-Goddard Global Ozone Chemistry Aerosol Radiation and Transport (GOCART) model as implemented in WRF-Chem v4.1. Our analysis focused on a convective dust event case study from 3-4 July 2014 for the southwest United States desert region discussed by other published works. Previous studies have found that WRF-Chem simulations grossly overestimated the dust transport associated with this event. Our results show that removing the default erodibility map and adding the drag parameterization to the AFWA dust module markedly improved the overall magnitude and spatial pattern of simulated dust conditions for this event. Simulated PM_{10} values near the leading edge of the storm substantially decreased in magnitude (e.g., maximum PM_{10} values reduced from 17,151 μg m^{-3} to 8,539 μg m^{-3}), bringing the simulated results into alignment with the observed PM_{10} measurements. Furthermore, the addition of the drag partition restricted the erroneous widespread dust emission of the original model configuration. We also show that similar model improvements can be achieved by replacing the wind friction speed parameter in the original dust emission module with globally-scaled surface wind speeds, suggesting that a well-tuned constant could be used as a substitute for the albedo-based product for short-duration simulations where surface roughness is not expected to change and for landscapes where roughness is constant over years to months. Though this alter-

native scaling method requires less processing, knowing how to best tune the model winds *a priori* could be a considerable challenge. Overall, our results demonstrate how dust transport simulation and forecasting with the AFWA dust module can be improved in vegetated drylands by calculating the dust emission flux with surface wind friction speed from a drag partition treatment.

1 Introduction

Surface roughness features such as rocks, vegetation, and soil ridges created by tillage attenuate wind flow over the soil surface, considerably affecting aeolian sediment transport and dust emission patterns (see reviews by Mayaud and Webb, 2017; Shao et al., 2015). Representing aerodynamic roughness effects and their spatiotemporal dynamics effectively in numerical dust models is, therefore, critical for estimating and forecasting the spatial patterns, timing, magnitude, and frequency of mineral dust emission accurately (Evans et al., 2016; Fu, 2019; Ito and Kok, 2017; Li et al., 2013; Tegen et al., 2002; Webb et al., 2014a, b). Several methods are available for characterizing vegetation effects in dust emission models (e.g., Evans et al., 2016; Ginoux et al., 2001; Ito and Kok, 2017; Kim et al., 2013; King et al., 2005; Koven and Fung, 2008; Marticorena and Bergametti, 1995; Okin, 2008; Raupach et al., 1993; Tegen et al., 2002). However, many of these techniques require in situ data that are challenging to obtain over large spatial footprints or incorporate parameterizations with dependencies on land use or vegetation datasets that are often out of date or fail to represent the complex three-dimensional heterogeneity of landscape roughness elements (e.g., Pierre et al., 2014; Raupach et al., 1993).

Tuning dust models to satellite- and ground-based observations of dust concentrations and dust optical depth have generally been sufficient approaches for making dust models useful for large-scale climate and air quality applications (e.g., Cakmur et al., 2006). These particular applications tend to focus on total atmospheric dust aerosol loading trends instead of individual dust events. If the goal is to capture the general magnitude and frequency of large-scale dust aerosol patterns, tuning practices are often a viable solution to simulated dust emission errors. However, the relatively poor representation of surface roughness effects on wind erosivity in current dust models has limited our capacity to forecast individual dust events accurately in desert regions with vegetation. Furthermore, poor roughness effect representation limits our ability to accurately simulate the influence of land management practices and desertification on spatial and temporal patterns of dust emission (Webb and Pierre, 2018).

Sediment mobilization schemes are often represented in terms of wind friction speed, u_*, a scalar parameter commonly used to describe processes related to wind shear stress (τ; note that $\tau = \rho(u_*)^2$, and ρ is air density). Near the land surface, u_* represents the total wind shear stress (τ) acting on both the horizontal soil surface (τ_s) and roughness elements (τ_r) (i.e., $\tau = \tau_s + \tau_r$; see Raupach, 1992; Raupach et al., 1993). This process is typically termed *drag partitioning* and is often expressed in terms of u_* rather than τ. Since τ is proportional to u_*, we can similarly divide u_* into soil surface (u_{s*}) and roughness (u_{r*}) components (i.e., $u_* = u_{s*} + u_{r*}$). The wind shear stress that reaches the immediate soil surface (i.e., τ_s) governs particle mobilization, so dust emission models driven by u_{s*} (or wind erosivity) instead of u_* may produce better outcomes (e.g., Darmenova et al., 2009; Okin, 2008; Webb et al., 2020). However, this assumption is worth testing for individual modeling applications since more physically sophisticated methods do not always lead to better simulation outcomes, especially when

the more advanced modeling approaches are limited by uncertainties in their required input parameters (e.g., LeGrand et al., 2019).

Though roughness elements affecting u_{s*} could comprise any ground feature obstructing airflow over the land surface, traditional aeolian transport models generally equate roughness to vegetation cover, with varying degrees of sophistication in their approach. For example, some models restrict or reduce dust fluxes based on static prescribed vegetation or land use attributes (e.g., Ginoux et al., 2001; LeGrand et al., 2019; Woodward, 2001). Others implement dynamic masks or spatially-varying dust flux scaling factors based on real-time or climatological datasets derived from greenness fraction, Leaf Area Index, or Normalized Difference Vegetation Index satellite data (Asadov and Kerimov, 2019; Collins et al., 2011; Evans et al., 2016; Ito and Kok, 2017; Kim et al., 2013; Kok et al., 2014; Solomos et al., 2019; Spyrou et al., 2022; Tegen et al., 2002; Vukovic et al., 2014). While some of these techniques have proven useful in certain modeling applications, they depend on datasets that primarily highlight plant productivity phases (e.g., Yu et al., 2016), which may not translate well to soil surface sheltering (Okin, 2010).

Chappell and Webb (2016) proposed a method for parameterizing u_{s*} in aeolian transport models using remotely-sensed surface albedo (ω). Their technique infers the drag partition from shadows (1-ω) cast by roughness elements based on the assumption that shadows can serve as a proxy for the sheltered surface area extent (Chappell et al., 2010). As described in Ziegler et al. (2020), a generalizable form of the Chappell and Webb (2016) approach equates to:

$$u_{s*} = u_{ns*}U_{10\text{m}}, \tag{1}$$

where $U_{10\text{m}}$ is the wind speed 10 m above ground level, and u_{ns*} is a normalized u_{s*} parameter (unitless) derived from albedo. By using an albedo-based calculation for each pixel area, the Chappell and Webb (2016) method provides an areal estimate of u_{s*} for both the sheltered and non-sheltered zones of the soil surface within each grid pixel.

Here, we explore the use of the Chappell and Webb (2016) albedo-based drag partition within the Weather Research and Forecasting model with Chemistry (WRF-Chem). WRF-Chem is a physically-based Earth-system model that simulates atmospheric motion on a non-hydrostatic, Eulerian grid in addition to the emission, transport, and mixing of gases and aerosols simultaneously with the meteorology (Fast et al., 2006; Grell et al., 2005; Peckham et al., 2017; Skamarock et al., 2019). The WRF-Chem framework is configurable and can be run with a variety of aerosol and atmospheric chemistry parameterizations, depending on a user's specific interests and computational resources. For this effort, we chose to use the AFWA dust emission module (LeGrand et al., 2019) with the Georgia Institute of Technology–Goddard Global Ozone Chemistry Aerosol Radiation and Transport (GOCART) model (Chin et al., 2000; Ginoux et al., 2001) as implemented in WRF-Chem v4.1.

The AFWA dust emission equations assume wind-driven dust entrainment primarily occurs through a process called saltation bombardment, in which wind-lofted sand-sized particles ($\sim$50 – 2000 μm diameter) too heavy to remain suspended in the air collide with the land surface and eject smaller dust-sized particles (generally $<$ 20 μm diameter) upon impact (e.g., Gillette, 1977; Kok et al., 2012). Several studies have investigated the use of the AFWA dust emission module for a variety of dust modeling applications (e.g., Aragnou et al., 2021; Francis et al., 2022; Hamzeh et al., 2021; Karumuri et al., 2022; Kuchera et

al., 2021; Mesbahzadeh et al., 2020; Miller et al., 2021; Mohebbi et al., 2019; Péré et al., 2018; Saidou Chaibou et al., 2020; Solomos et al., 2018; Teixeira et al., 2016; Tsarpalis et al., 2018, 2020; Uzan et al., 2016; Xu et al., 2017; Zhang et al., 2022; Zhou et al., 2019). In general, these studies highlight useful applications of the model. However, several authors noted the need for improved dust source and land surface characterizations in regions with heterogeneous terrain (Cremades et al., 2017; Fountoukis et al., 2016; Hyde et al., 2018; Kim et al., 2021; Ma et al., 2019; Mohebbi et al., 2020; Nabavi et al., 2017; Nguyen et al., 2019; Nikfal et al., 2018; Parajuli et al., 2019, 2020; Parajuli and Zender, 2018; Rizza et al., 2016, 2021; Spyrou et al., 2022; Su and Fung, 2015; Yuan et al., 2019; Zhao et al., 2020).

Here, we aim to evaluate the sensitivity of dust transport simulated by WRF-Chem to the Chappell and Webb (2016) albedo-based drag partition. Our analysis focused on a convective dust event case study from 3-4 July 2014 for the desert southwest U.S. region previously discussed by other published works (e.g., Hyde et al., 2018; Yu and Yang, 2016). The results from Hyde et al. (2018), in particular, motivated our case study choice. They found that the AFWA dust emission scheme used in WRF-Chem grossly overestimated dust transport for this event. We hypothesized that better geographic sheltering-effect representation from the Chappell and Webb (2016) drag partition would improve the overall magnitude and spatial pattern of the emitted dust and ultimately result in an improved simulation of transported dust. This hypothesis is further strengthened by recent findings from Bukowski and van den Heever (2022), who found accurate roughness effect characterizations are critical for predicting dust patterns associated with cold pool events similar to our chosen case study.

2 Methodology

2.1 Dust emission flux calculation

The AFWA dust emission module (LeGrand et al., 2019) is an adaptation of the dust emission scheme originally described by Marticorena and Bergametti (1995). Equations comprising the AFWA code are in terms of u_* and primarily include the threshold friction speed required for particle entrainment over an idealized smooth surface (u_{*ts}), the horizontal saltation flux (Q), the bulk vertical dust flux (F_B), and the size-resolved emitted dust flux. For a detailed overview of the dust emission module equations, see LeGrand et al. (2019). The following two sub-sections summarize the main components of the AFWA dust emission model and the modifications required to incorporate the Chappell and Webb (2016) drag partition.

2.1.1 The original AFWA module configuration

In the AFWA dust emission calculation, soil particles are divided into a predetermined number of bins based on their effective particle size (referred to as size bins). Tables 1-2 provide attributes associated with the nine size bins used for saltation-based processes and the five size bins used for emitted dust. Here, we denote effective diameters for saltation and dust particles by $D_{s,p}$ and $D_{d,p}$, respectively.

As the simulation evolves, saltation for a given size bin initiates and ceases as u_* exceeds or falls below size-resolved values of u_{*ts}, respectively. First, the module generates a semi-empirical u_{*ts} estimate (in units of centimeters per second) for each saltation size bin, $u_{*ts}(D_{s,p})$, assuming air-dry soil conditions:

$$u_{*ts}(D_{s,p}) = 0.13 \frac{\left(\frac{\rho_{s,p} g D_{s,p}}{\rho_a}\right)^{0.5} \left(1 + \frac{0.006}{\rho_{s,p} g D_{s,p}^{2.5}}\right)^{0.5}}{\left[1.928 \left(a_{mb}(D_{s,p})^x + b_{mb}\right)^{0.092} - 1\right]^{0.5}}, \tag{2}$$

where g = 981 cm s^{-2} is the gravitational constant, ρ_a is the spatiotemporally varying air density from the lowest model atmospheric layer, $\rho_{s,p}$ is the particle density of saltation bin p, $x = 1.56$, $a_{mb} = 1331$ cm^{-x}, and $b_{mb} = 0.38$. The code then applies a correction function, $f(\theta)$, that incorporates soil water content and clay composition to account for the effects of soil moisture on particle cohesion based on the approach of Fécan et al. (1999):

$$u_{*ts}(D_{s,p}, \theta) = u_{*ts}(D_{s,p}) f(\theta). \tag{3}$$

Next, the module diagnoses size-resolved saltation flux ($Q(D_{s,p})$: in units of grams per centimeter per second) values for each saltation size bin following,

$$Q(D_{s,p}) = \begin{cases} C\frac{\rho_a}{g} u_*^3 \left(1 + \frac{u_{*ts}(D_{s,p},\theta)}{u_*}\right)\left(1 - \frac{u_{*ts}(D_{s,p},\theta)^2}{u_*^2}\right), & u_* > u_{*ts}(D_{s,p},\theta) \\ 0, & u_* \leq u_{*ts}(D_{s,p},\theta) \end{cases}, \tag{4}$$

where C is an empirical proportionality constant set to 1.0. The module then multiplies $Q(D_{s,p})$ by bin-specific weighting factors (dS_{rel}) determined from prescribed mass distribution assumptions and spatially varying sand, silt, and clay mass fractions. The integrated sum of the weighted $Q(D_{s,p})$ values determines the total streamwise saltation flux, Q, associated with each model grid cell:

$$Q = \sum_{s,p=1}^{9} Q(D_{s,p}) dS_{rel}(D_{s,p}). \tag{5}$$

After determining Q, the module generates the bulk vertical dust emission flux (F_B; in units of grams per centimeter squared per second) triggered by saltation by multiplying the Q field by a topographic-based dust source strength parameter (S) and a sandblasting efficiency factor (β; in units of value per centimeter) derived from the soil clay fraction. The F_B calculation also includes an aerodynamic roughness length (z_0) conditional to limit dust emission to non-urban regions with relatively sparse vegetation coverage:

$$F_B = \begin{cases} QS\beta, & z_0 \leq 20 \text{ cm} \\ 0, & z_0 > 20 \text{ cm} \end{cases}, \tag{6}$$

where

$$\beta = \begin{cases} 10^{0.136(m_{\text{clay}})-6}, & m_{\text{clay}} < 0.2 \\ 1.06 \times 10^{-6}, & m_{\text{clay}} \geq 0.2 \end{cases}, \tag{7}$$

and m_{clay} is the soil clay mass fraction. Here, z_0 represents the theoretical height at which the mean wind speed near the surface falls to zero due to surface-induced drag (e.g., Stull, 1988; Zobeck et al., 2003). Importantly, this z_0 parameter is not part of the new drag partition treatment, but rather a value from the parent WRF model used for a variety of land surface and air flow processes and diagnostics.

Effectively, the m_{clay} conditional in Eq. (7) limits the sandblasting efficiency parameter to 1.06×10^{-6} cm^{-1} when the soil composition exceeds 20% clay content. However, as noted by LeGrand et al. (2019), the β function primarily serves as a dimensional scaling factor. The overall effects of soil clay content variability on F_B are relatively small.

The S parameter (originally described by Ginoux et al., 2001) represents the availability of loose erodible soil material at a given location based on the degree of topographic relief of the surrounding area. This approach assumes that soil composition remains consistent over time, and the simulated land surface will neither run out of dust material nor acquire new dust material through fluvial or atmospheric deposition as the simulation evolves. Some papers refer to this spatially varying S field as an erodibility or dust source map. However, both labels provide an inaccurate description of how S functions in the AFWA module. Accordingly, we will not use that terminology here. Essentially, S is a spatially varying tuning parameter ranging from 0 to 1 that assumes erodible material accumulates in low points in the terrain, determined by:

$$S = \left(\frac{z_{\text{max}} - z_i}{z_{\text{max}} - z_{\text{min}}} \right)^5, \tag{8}$$

where z_i is the elevation of the cell, and z_{max} and z_{min} are the maximum and minimum terrain elevation in the surrounding $10°$ $\times$ $10°$ area, respectively.

Of note, the AFWA module uses interpolated values of S initially derived from a $\frac{1}{4}°$ elevation dataset. In addition, the S field incorporates a static vegetation mask that blocks dust emission (i.e., $S = 0$) from vegetated areas derived from a $1° \times 1°$ resolution land cover dataset. While these settings may be appropriate for some modeling applications, the coarse nature of these input datasets likely limits the spatial viability of S at mesoscale and convective-permitting model resolutions (e.g., Saleeby et al., 2019; Vukovic et al., 2014; Walker et al., 2009).

Next, the module applies a prescribed particle size distribution derived using the Kok (2011) brittle fragmentation theory to obtain size-resolved dust emission fluxes:

$$F(D_{d,p}) = F_B \kappa (D_{d,p}), \tag{9}$$

where $F(D_{d,p})$ is the size-resolved emitted dust flux (in units of grams per centimeter squared per second) and $\kappa_{d,p}$ is the distribution fraction of the suspended dust size bin (see Table 2). Lastly, the AFWA module uses $F(D_{d,p})$ values to determine

the size-resolved dust concentrations injected into the first model atmospheric level for transport during each model time step. From this point forward, functions from other modules in the GOCART suite take over processing the fate and transport of the airborne dust aerosols.

2.1.2 Incorporation of drag partitioning

175 To obtain gridded values of u_{ns*} for use in WRF-Chem, we estimated surface shadowing using data from the snow-masked 500 m Moderate Resolution Imaging Spectroradiometer (MODIS) Bidirectional Reflectance Distribution Function (BRDF) albedo daily product (Collection 6, MCD43A1). Following Chappell and Webb (2016) and Ziegler et al. (2020), we derived the normalized proportion of shadow (represented using a normalized albedo, ω_n) by:

$$\omega_n = \frac{1 - \omega_{\mathrm{dir}}(0°)}{f\mathrm{iso}},$$ (10)

180 where $\omega_{\mathrm{dir}}(0°)$ is the daily nadir "black-sky" albedo for MODIS band 1 (620-670 nm wavelength) and f_{iso} is the band 1 BRDF isotropic weighting parameter. In essence, Eq. (10) integrates the albedo across viewing angles for a single illumination angle (solar noon), producing an areal shadow estimate that, in theory, represents non-erodible roughness element conditions for an integrated (500 m pixel) area (e.g., Fig. 1 from Ziegler et al., 2020). We then determined daily u_{ns*} by:

$$u_{ns*} = 0.0311 \left(\exp \frac{-\omega_{ns}^{1.131}}{0.016} + 0.007 \right),$$ (11)

185 where ω_{ns} represents an empirically-scaled proportion of shadow obtained via:

$$\omega_{ns} = \frac{(a - b)(\omega_n - 35)}{-35} + b,$$ (12)

using the scaling factors a = 0.0001 and b = 0.1 to align ω_{ns} with the ray-casting performed on the reconstructed roughness element configurations in the wind tunnel study by Marshall (1971).

To incorporate u_{s*} into the AFWA dust emission module, we configured WRF-Chem to ingest daily MODIS-derived u_{ns*}

190 fields (Eq. (11)) that had been interpolated to the model grid domain into the WRF-Chem framework through an auxiliary channel at model run time and modified the dust emission equations to use u_{s*} in place of u_*. We then converted daily u_{ns*} values to instantaneous u_{s*} estimates following Eq. (1), using the WRF-Chem simulated wind speed at 10 m above ground level that updates each model time step as $U_{10\mathrm{m}}$. Finally, we replaced u_* in the saltation function from Eq. (4) with u_{s*}:

$$Q(D_{s,p}) = \begin{cases} C\frac{\rho_a}{g}u_{s*}^3 \left(1 + \frac{u_{*ts}(D_{s,p},\theta)}{u_{s*}}\right)\left(1 - \frac{u_{*ts}(D_{s,p},\theta)^2}{u_{s*}^2}\right), & u_{s*} > u_{*ts}(D_{s,p},\theta) \\ 0, & u_{s*} \leq u_{*ts}(D_{s,p},\theta) \end{cases}.$$ (13)

195 Note that estimated dust emissions are particularly sensitive to small changes in wind friction speed due to the cubed component of the saltation equation (e.g., Tegen et al., 2002). This replacement of u_* with u_{s*} in Eq. (13) makes the saltation

equation consistent with the physics of aeolian transport in the presence of roughness, where excess wind friction speed at the soil surface (i.e., friction speed above the threshold required for particle mobilization) governs the saltation mass flux (Webb et al., 2020). In addition, we added model run-time configuration options to disable the z_0 conditional and remove the S factor from the F_B function (Eq. (6)) since both of these features incorporate broadscale vegetation masks. Readers are encouraged to review the report by Michaels et al. (2022) for a detailed overview of the code implementation process and model run-time instructions.

The use of the snow-masked version of the MODIS product is essential for this particular modeling application. Although the AFWA module restricts dust emissions from snow-covered areas, the snow-covered grid spaces in the model may not align with snow-covered pixels in the MODIS product. Accordingly, our model implementation process assumes $u_{s*} = 0$ m s^{-1} for grid spaces with missing data in the MODIS product. This assumption effectively blocks dust emissions from MODIS-detected snow-covered regions and water bodies. We note the potential for missing data problems if the MODIS retrievals have poor spatial coverage. If this scenario occurs, we recommend users consider filling the gaps through interpolation techniques (assuming the missing data gaps are minimal), using seasonal or monthly climatological u_{ns*} values, or using a u_{ns*} input dataset from a previous period.

2.2   Description of case study event

As described in detail by Gallagher et al. (2022), our case study dust event was driven by a convective outflow boundary associated with a thunderstorm cluster that developed and evolved over central and southern Arizona following convective weather patterns characteristic of the North American Monsoon's summer phase (e.g., Adams and Comrie, 1997). The event began at 1800 UTC on 3 July 2014, peaked at around 0000 UTC on 4 July 2014, and concluded mainly by 1200 UTC on 4 July 2014. At the peak of the event, convective cells organized into an extensive north-south line, pivoting clockwise about its northern end. By 4 July 2014, 0200 UTC, the convective line collapsed into three components, with each portion progressing in different directions as they diverged. The gust front associated with the central cell just south of Phoenix, Arizona generated a thick wall of dust that preceded the storm as it continued west-northwest over the metropolitan area. Figure 1 provides a conceptual overview of the general environmental forcing conditions associated with the dust event. For a more in-depth review of the storm evolution, including synoptic, mesoscale, and local condition assessments using a broad collection of analysis fields, radar composites, and observations for support, we encourage readers to review the Gallagher et al. (2022) report.

Our simulation analysis primarily focused on dust produced by the cell that affected Phoenix. However, we also chose this particular case study because dust concentrations outside the immediate Phoenix area were relatively low in magnitude or negligible. The model's ability to simulate minimal dust loading and dust-free (i.e., clear sky) conditions accurately is also important for it to be a reliable prediction tool. For the simulated results to be considered successful for this case study, the model should be able to both capture the progression of the dust wall over Phoenix and limit dust production from the rest of the broader model domain.

2.3 Model configuration

WRF-Chem is a version of the Weather Research and Forecasting (WRF) model by Skamarock et al. (2019) with additional modules for atmospheric chemistry processes and feedbacks (Fast et al., 2006; Grell et al., 2005). Like WRF, WRF-Chem is a fully compressible finite difference model that simulates atmospheric motion on the Arakawa C-grid and incorporates a variety of parameterizations for simulating sub-grid atmospheric motion, cloud microphysics, radiation, and terrain processes. We used WRF-Chem v4.1 for our test case simulation with WRF parent model configuration settings suggested by Gallagher et al. (2022) and chemistry settings from LeGrand et al. (2019) and Letcher and LeGrand (2018). The study by Gallagher et al. investigated the sensitivity of WRF-simulated atmospheric forcing conditions for the dust event studied here. In particular, they focused on the effects of model initialization (spin-up) time, initial atmospheric conditions, horizontal and vertical model resolutions, and several WRF physics package settings to determine the optimal model configuration that minimized environmental forcing condition errors on the dust simulation.

Table 3 provides a brief overview of the model chemistry and physics configuration. However, complete pre-processor and run-time configuration files (referred to as the namelist.wps and namelist.input files, respectively) for this effort are available from the code repository by Letcher et al. (2022) and in the report by Michaels et al. (2022). The model vertical grid used the default spacing distribution with 40 levels following a stretched hybrid sigma-pressure vertical coordinate that favors higher resolution near the ground. We note that the text and Table 2 from Gallagher et al. (2022) erroneously list their model configuration as having 42 vertical levels instead of 40. However, we confirmed their study simulations were generated with the same vertical level configuration used for our assessment. Figure 2 displays the three telescoping model domains (D01, D02, and D03, hereafter) with grid resolutions of 18 km, 6 km, and 2 km, respectively. In Fig. 3-4, we show key terrain attributes associated with the AFWA dust emission functions for D02 and D03, which primarily encompass the southwest U.S. desert region.

We set the WRF-Chem initial and lateral boundary forcing conditions using 3-hourly analysis fields from the Rapid Refresh Model (Benjamin et al., 2016) supplemented with 6-hourly soil moisture information from the National Centers for Environmental Prediction North American Model analysis product. Though these data are obtainable from multiple resources, we acquired all of our forcing datasets from the National Center for Environmental Information data portal: https://www.ncdc.noaa.gov/data-access/model-data/model-datasets (last access: 20 November 2019).

We performed our simulations for a two-day period from 3 July 2014, 0000 UTC to 5 July 2014, 0000 UTC (2 July 2014, 1700 LT to 4 July 2014, 1700 LT for Arizona). The first 12 hours of the simulation (0000-1200 UTC 3 July 2014) were disregarded as spin-up to allow the model to adjust to the initial and lateral boundary conditions. Atmospheric dust was initialized using a "cold start" approach, which assumes an initial atmospheric dust concentration of zero. Settings engaged by the GOCART simple option in WRF-Chem generated atmospheric fields for other non-dust aerosols, including sea salt, black carbon, organic carbon, and dimethyl sulfide. This particular configuration assumes background sea salt emissions based on the lowest model level wind speeds over the oceans (Gong, 2003) and emissions for the other three aerosol species using climatological emission datasets and the WRF-Chem PREP-CHEM-SRC preprocessing software (Freitas et al., 2011). All dust

aerosols originated from the local model domain, meaning that no additional dust aerosols entered the D01 lateral boundaries
265 as the simulations evolved. We consider this a reasonable assumption given the relatively short duration of the case study and
because the dust event generated from localized, convection-induced conditions well within the D01 boundaries.

To better understand the sensitivity of the model to the drag partition treatment, we assessed five test configurations, including
a simulation produced using the original AFWA code configuration without a drag partition as a control (CTRL) and four
alternative versions using the modified size-resolved saltation treatment from Eq. (13) (see Table 4). The first alternative
270 configuration (ALT1) applied the u_{s*}-based $Q(D_{s,p})$ estimates and the original F_B calculation (Eq. (6)), which restricts dust
emission from grid cells classified by the model as areas with z_0 greater than 20 cm. Because we used the model default 21-class
MODIS International Geosphere-Biosphere Programme (IGBP) dataset to characterize land use, this conditional effectively
limits dust production to areas classified by the model as barren, grassland, shrubland, savanna, or cropland. The second
alternative configuration (ALT2) is identical to ALT1 but with the z_0 conditional removed. Our third alternative configuration
275 (ALT3) further simplifies ALT2 by removing the preferential source strength term from the F_B calculation (i.e., $S = 1$). Lastly,
the fourth alternative configuration (ALT4) estimates u_{s*} by applying a global scaling factor (C_s) to U_{10m}:

$$u_{s*} = C_s U_{10m}, \tag{14}$$

with C_s set to a value within the general range of u_{ns*} values estimated for the model domain by Eq. (11). Similar to ALT3, the
ALT4 configuration also ignores the the z_0 conditional and assumes $S = 1$.
280 The ALT3 configuration tested the ability of the albedo-based approach to accurately represent the spatially varying surface
aerodynamic sheltering afforded by non-erodible roughness elements on the land surface. However, we specifically included
the ALT4 configuration to test if the model is able to achieve similar results for this case study event by using globally
scaled surface winds without the additional input data acquisition and preprocessing requirements inherent to the Chappell
and Webb (2016) method. In other words, ALT4 explores if a model user could achieve the same outcome as the Chappell
285 and Webb (2016) drag partition scheme by simply tuning down the winds if the dust source areas in their domain of interest
were generally prone to coverage by vegetation or other roughness elements. Effectively, ALT3 and ALT4 are the only model
configurations without some form of vegetation mask built into the dust emission code (see Fig. 5).

Figure 6 provides a comprehensive schematic summary of the five test configurations and their required input parameters.
This multi-tiered testing approach enabled us to explore the drag partition's influence on simulation outcomes systematically.
290 The z_0 dependency removal is relatively straightforward since it primarily serves as a vegetation mask. However, omitting
the S parameter also removes the spatially varying available sediment supply tuning parameter from Eq. (6). Since the drag
partition provides no direct information about sediment supply, it is not clear if removing S is a universally valid approach. We
note, however, that previous studies have found that the default WRF-Chem S parameter provides a poor representation of dust
source strength in our case study area (e.g., Vukovic et al., 2014; Parajuli and Zender, 2018). Setting S to 1 forces the model to
295 assume that all areas are functionally equally erodible and that dust emissions are solely a result of saltation and sandblasting

efficiency. Replacing the built-in WRF-Chem S field without the static vegetation mask, though, is beyond the scope of this effort.

Note that β, in this case, is homogenous in the study area (e.g., Fig. 4f) due to the relatively clay-rich soil content of the region (e.g., Fig. 4b) and is capped at 1.06×10^{-6} cm^{-1} everywhere the soil composition exceeds 20% clay content (e.g., Fig. 4c). Accordingly, we can assume that the resultant simulated dust emission patterns produced by our test configurations are a function of Q, S, the z_0 mask, or some combination of these parameters.

2.4 Observation data

We evaluated model performance using in situ observations from Automated Surface Observing Stations (ASOS). ASOS observations are available in standard Meteorological Aerodrome Report (METAR) format (e.g., WMO, 2018) every hour and in the less conventional one-minute or five-minute format, depending on the station. Gallagher et al. (2022) previously assessed model wind speed for our simulation configuration in the vicinity of the main event convection using one-minute frequency ASOS data. Thus, our analysis primarily focused on comparing simulated data against ASOS present weather and visibility observations and wind speed measurements for ambient conditions away from the main convective dust event using ASOS data accessed through the Meteorological Assimilation Data Ingest System (MADIS) portal (https://madis.ncep.noaa.gov, last access: 12 November 2021). We also compared simulated results against observed concentrations of particulate matter up to 10 μm in diameter (PM$_{10}$) using hourly PM$_{10}$ in situ measurements obtained from the U.S. Environmental Protection Agency's Air Quality System database (retrieved via an application programming interface at https://www.epa.gov/outdoor-air-quality-data, last access: 1 July 2020). We did not consult additional satellite-retrieved products like false color dust-enhanced imagery and aerosol optical depth to supplement our assessment due to cloud obscuration over the area of interest.

To evaluate simulated storm structure, location, and timing, we analyzed observed Next Generation Weather Radar (NEXRAD) composite imagery (available at https://www.ncdc.noaa.gov/nexradinv/, last access: 1 July 2020) to qualitatively compare and verify the location, structure, and intensity of the simulated convective storms. The radar composite images comprise a blend of radar reflectivity from individual locations with overlapping coverage to generate a cohesive radar map across the continental United States. This mosaic approach has the advantage of filling in blockages from individual radar sites with neighboring ones, providing a more complete snapshot of convective activity across the radar network coverage area.

3 Results

Experimental results are reviewed as follows. We begin with an overview of the u_{ns*} field, then review the environmental forcing conditions and dynamic components of the dust emission scheme simulated by the model. Lastly, we assess the resultant dust-related parameters produced by each test configuration outlined in Table 4. This holistic component-based approach helps to break down how the many factors affecting modeled dust conditions contributed to each test simulation outcome.

3.1 Albedo-derived normalized surface friction speed

Figure 7 shows the normalized surface wind friction speed for the case study period diagnosed from MODIS BRDF data and Eq. (11) interpolated to the model domain. Although we consider u_{ns*} to be a dynamic parameter, u_{ns*} here is a static field (i.e., u_{ns*} only varies spatially, not temporally) due to the relatively short duration of our case study simulation (48 hours). Note, the u_{ns*} values in the areas characterized by the model as shrubland range from 0.0225 to 0.0325, barren areas are around 0.03 to 0.035, croplands are 0.0125 to 0.02, and forested and urban areas generally range from 0.005 to 0.0225. The upper limits of u_{ns*} associated with forested and urban areas are likely higher than those of croplands due to roughness element height consistency and density. For example, plants in individual crop fields generally grow at relatively uniform rates and spacing, giving the crop canopy a "smoother" aerodynamic roughness than urban centers and forested regions with more heterogeneity in roughness element height, shape, and density.

3.2 Environmental forcing conditions

We conducted a rigorous evaluation of the simulated environmental forcing conditions so we could account for any wind flow errors in our assessment of simulated PM_{10} against hourly station-based PM_{10} measurements. The model was able to reproduce the storm's general structure and timing, including the formation of the initial quasi-linear convective system and the collapse of the convective line into individual cells (results consistent with findings by Gallagher et al., 2022). Furthermore, the simulated near-surface wind speeds were in good agreement with wind speeds observed at ASOS stations. However, simulated wind speeds peaked 1 to 2 hours early in some locations with slightly higher (about +1 m s^{-1}) intensity. According to Gallagher et al., these minor wind speed errors may be partly due to erroneous land use characterization, particularly in the higher terrain elevation areas where the storm initiated. Gallagher et al. also performed a full statistical analysis of simulated surface wind speeds against all available ASOS wind speed data from the innermost domain (D03). The average wind speed bias for the entire forecast period was +0.59 m s^{-1}. However, a large portion of this overestimation occurred during non-convective nocturnal periods (3 July, 0500–1500 UTC and 4 July, 0800–1600 UTC).

To better assess the potential influence of these minor errors in wind flow on simulated dust concentrations, we conducted a more in-depth review of the location and timing of the primary cell that produced the main dust event. Specifically, we examined locational differences between a central point along the storm's leading edge in both the observed- and modeled-radar reflectivity over the dust-producing cell's lifetime (Fig. 8). Overall, the simulated convective activity developed and propagated more northwest than the patterns we observed in the composite radar images. This divergence began with a slight difference in where the cells initiated, followed by a more prevalent westward motion in the simulated conditions than the storm's actual southwest track. As the storm's evolution continued, the simulated event maintained its path and velocity while the observed event pivoted and accelerated. Though variation between the simulated and actual storm tracks occurred, this distance became smaller over time (Fig. 8c).

Due to these discrepancies, we must limit our simulated dust assessment to a qualitative evaluation of the overall storm system rather than comparing hourly simulated time series of PM_{10} to observed values associated with an exact geospatial

point. This approach, however, is not inconsistent with convective weather analyses since simulating the precise placement

360 and timing of individual convective cells is generally considered more luck than skill due to irreducible limitations in non-linear model physics, numerical processing, and initialization accuracy. Capturing the general spatial pattern and timing of the dust event is the higher priority as model users can often correct persistent magnitude errors through global model tuning parameters.

Simulated time series of U_{10m}, u_*, and albedo-derived u_{s*} values associated with the peak of the dust event (4 July 2014,

365 0000–0300 UTC) are provided in Fig. 9. Overall, the U_{10m} patterns align well with the ASOS station observations and areas of convective activity seen in the radar composite imagery (see supplemental Fig. S1). We note that the simulated u_* values are generally an order of magnitude stronger than their associated u_{s*} partition. This outcome is likely due to the drag partitioning scheme interpreting the relatively "dark" terrain surfaces of the domain landscape (presumably caused by the prevalence of shrubs and grasses or trees) as areas with substantial roughness element coverage.

370 Figure 9 also shows time series of the threshold friction speed for air-dry soil conditions, the soil moisture-based correction function, and the soil wetness-corrected threshold friction speed for a particle with a diameter of 69 μm ($u_{*ts}(D_{s,p} = 69$ μm), $f(\theta)$, and $u_{*ts}(D_{s,p} = 69$ μm, $\theta)$, respectively). This particular particle size is the effective diameter for saltation size bin 7 (see Table 1). As described in a review paper by Kok et al. (2012, and references within), the u_{*ts} parameter represents the minimum surface wind shear stress needed to overcome the inertial, cohesive, and adhesive forces holding the particle to the soil bed.

375 Interparticle forces (e.g., capillary, Van der Waals, electrostatic, chemical binding, and coulomb forces) keeping the particles fixed to the ground have a stronger effect on smaller particles due to their high ratio of surface area to volume. However, larger particles require more energy from the wind to mobilize because inertial force effects become stronger with increasing particle mass. The $u_{*ts}(D_{s,p})$ curve produced by Eq. (2) has a minimum of about 74 μm (assuming standard atmospheric pressure of 1225 kg m^3) because fine sand grains are less subject to interparticle forces than smaller clay- and silt-sized particles but are still

380 relatively lightweight. Hence, fine sand-sized particles tend to be the first particles to mobilize from direct wind shear stress. Accordingly, particles associated with saltation size bin 7 ($D_{s,p} = 69$ μm) in the AFWA module will be the first to mobilize. Thus, we consider spatial patterns related to saltation size bin 7 to be good diagnostic indicators of overall dust emission model behavior.

Air density is the only spatiotemporally varying parameter in the calculation of $u_{*ts}(D_{s,p})$. Though we can discern a slight

385 reduction in $u_{*ts}(D_{s,p} = 69$ μm) over time immediately under the convective line (Fig. 9m-p), the overall effect of air density on $u_{*ts}(D_{s,p})$ for this case is relatively negligible. Under air-dry soil conditions, $u_{*ts}(D_{s,p} = 69$ μm) ranges between 0.17 to 0.19 m s^{-1} across most of the domain. These results also align with findings by Darmenova et al. (2009) in their assessment of the sensitivity of the Marticorena and Bergametti (1995) dust emission scheme to uncertainties in its required input parameters.

We also see relatively little change in the $f(\theta)$ field during the dust event, except for the area associated with a line of

390 precipitation that occurred within the convective cell behind the main wall of dust (Fig. 9q-t). The $u_{*ts}(D_{s,p} = 69$ μm, $\theta)$ maxima over the Mogollon Rim align with isolated areas of convective precipitation that occurred earlier in the simulation (Fig. 9u-x). Note, however, that the $u_{*ts}(D_{s,p} = 69$ μm, $\theta)$ values along the Mogollon Rim adjacent to these maxima are around 0.2 to 0.3 m s^{-1}, comparable to $u_{*ts}(D_{s,p} = 69$ μm, $\theta)$ values in the southwest Arizona region where the dust event occurred,

and, for the most part, well below the simulated values of u_*. This particular aspect of the model behavior is important because the only component of the AFWA module preventing dust emissions from these drier forested areas in the ALT3 and ALT4 simulations is the drag partition treatment.

Figure 10 shows time series of the excess friction speed, u_{*ex}, for saltation size bin 7 associated with different treatments for particle mobilization during the peak of the event, where u_{*ex} is the model simulated friction speed driving the saltation and dust emission equations (i.e., u_* or u_{s*}) minus $u_{*ts}(D_{s,p} = 69 \; \mu m, \theta)$. The six examples provided in Fig. 10 include u_{*ex} calculated using the model-generated u_* values, u_{s*} values derived using the Chappell and Webb (2016) method (Eq. (1)), and four instances of u_{s*} values estimated from 10 m wind speeds scaled by a global tuning constant (C_s; Eq. (14)) as the wind forcing parameter. We considered values of C_s = 0.02, 0.025, 0.03, and 0.035 based on the general range of u_{ns*} values diagnosed for the area where the dust event occurred (e.g., Fig. 7; note, u_{ns*} has a theoretical maximum of 0.0381). Effectively, positive u_{*ex} values indicate that wind friction speeds are strong enough in the model to initiate particle mobilization, while negative u_{*ex} values imply the wind friction speeds are too weak. Immediately, we see that practically the entire domain is capable of lofting dust in the u_*-driven simulations if sufficient dust and saltator material are present (Fig. 10a-d). Conversely, dust production in the u_{s*}-driven simulations is restricted to isolated areas, including areas near the leading edges of individual storm cells (e.g., Fig. 10e-x). The u_{*ex} results generated with globally scaled U_{10m} and C_s = 0.025 (Fig. 10e-h) are markedly similar to the u_{*ex} values calculated with U_{10m} scaled by u_{ns*} (Fig. 10q-t). In particular, the excess friction speeds for these two instances match rather closely over Arizona, with minor spatial extent differences for positive u_{*ex} values in California and southern Nevada. Thus, we chose C_s = 0.025 as the U_{10m} global scaling constant for our ALT4 test configuration. Interestingly, areas in the u_{ns*} field equal to 0.025 (Fig. 7) tend to align with grid cells characterized as closed shrubland (Fig. 3) in the model domain where there were strong winds, though this may be a coincidence.

To further explore how our code modifications influenced simulated outcomes, we diagnosed time series of the horizontal saltation flux for the peak of the dust event associated with each test configuration (Fig. 11). Though the non-erodible area masking components of the AFWA dust emission code are not applied in the AFWA module until the F_B calculation (Eq. (6)), we included the appropriate non-erodible area masks for the CTRL, ALT1, and ALT2 configurations (see Fig. 5) in the Fig. 11 Q diagnostics. Strong saltation occurred everywhere in the CTRL configuration plots unless the grid spaces were masked out (e.g., Fig 11a-d). The four alternative model configurations showed similar Q patterns to each other, suggesting that the masking had little influence on the resultant Q flux in AFWA module configurations that accounted for drag partition. The ALT1 and ALT2 Q outcomes were practically identical because the z_0 > 20 cm mask largely coincides with the areas where S = 0 for this domain (e.g., Fig. 5). With the exception of a small area of saltation to the east of Phoenix, the ALT3 Q results are also similar to ALT1 and ALT2, which makes sense as developed/urban areas and higher-elevation forested regions generally yield low values of u_{ns*}. Lastly, the ALT4 Q spatial patterns mimic ALT3. However, the magnitude of the ALT4 Q flux in the areas outside of where the main dust event occurred are lower in magnitude than the ALT1, ALT2, and ALT3 results.

3.3 Simulated dust conditions

We compared our simulation results against observed PM_{10} concentrations (Fig. 12-14). To ensure our simulated PM_{10} conditions could primarily be attributed to dust transport, we also reviewed the general contribution of each aerosol species to the overall simulated PM_{10} patterns (not pictured). For this case, most of the simulated PM_{10} came from either dust or sea salt transport. Sea salt and dimethyl sulfide distributions were relatively isolated to areas over the ocean and the immediate coastlines, while dust was the primary source of PM_{10} over land. Contributions from black carbon, organic carbon, and dimethyl sulfide to simulated PM_{10} totals were negligible, except in dense urban areas along the southern California coastline.

Note that PM_{10} monitoring stations in the United States are generally situated around populated areas, so most of the PM_{10} sites associated with our model domain were tightly clustered around Phoenix (e.g., Fig. 13b). The dust wall crossed over the Phoenix metropolitan area between 0000 and 0400 UTC on 4 July 2014. Importantly, the air quality conditions rapidly recovered once the main dust wall passed, and the areas outside of the immediate dust event were relatively clear. According to surface weather station visibility, present weather records, and observer remarks for Arizona and southern California (not pictured), it is unlikely the strong dust obscurations extended much beyond the immediate convective cell outflow boundary area.

The original CTRL configuration produced a strong dust signal along the convective outflow boundary, but it also generated widespread dust concentrations in areas that in reality were clear (e.g., Fig. 12). Similar to the Q flux patterns, simulated PM_{10} concentrations produced by the ALT1 and ALT2 configurations were nearly identical because dust in the u_{s*}-driven simulations did not originate near a masked area (see Fig. 5). Due to this artifact, we opted to limit our PM_{10} assessment to the CTRL, ALT1, ALT3, and ALT4 simulations. The ALT1 configuration produced much lower PM_{10} concentrations than the other test settings, with some dust emerging near the gust front. The ALT1 "dust wall," however, was an order of magnitude lower than the observed conditions. In contrast, the magnitude and spatial pattern of the simulated PM_{10} values associated with ALT3 and ALT4 aligned better with reported observations.

Though the general PM_{10} patterns of the main dust event are similar between ALT3 and ALT4, the areas of maximum PM_{10} extend further south along the gust front in the ALT3 simulation than in the ALT4 version (Fig. 12). We also note higher PM_{10} values for ALT3 in southern California over the Mojave Desert and near the northeastern corner of Arizona compared to ALT4. However, the maximum PM_{10} values associated with these two areas occurred in observation-limited regions. PM_{10} observations from an EPA station in Barstow, California (Site ID: 06-071-0001; 34.8939080° N 117.024804° W) near the simulated area of maximum PM_{10} over the Mojave Desert suggest that simulated PM_{10} values in both ALT3 and ALT4 were higher than observed at this location (Fig. 14c). For example, simulated PM_{10} values for ALT3 and ALT4 at the Barstow site peaked at 570 and 346 μg m^{-3}, respectively, at 0000 UTC on 4 July 2014, while observed PM_{10} values ranged between 5 to 47 μg m^{-3} during the 4 July 2014, 0000-0400 UTC period. However, the PM_{10} concentrations in the simulations changed rapidly over short distances near the Barstow EPA station as the simulations evolved. Thus, small shifts in the simulated dust position could greatly affect the apparent skill of the simulated output.

Surface wind speed observations from Edwards Air Force Base (KEDW, K9L2), which is primarily upstream and west of
the simulated Mojave Desert PM_{10} plume, and Barstow (KDAG) suggest that there were strong wind speeds over the area in
question (Fig. 14). Observed wind speeds at the Barstow ASOS station closest to the simulated PM_{10} plume ranged from ~5 to
10 m s^{-1} between 0000-0300 UTC on 4 July 2014, which align relatively well with the modeled 10 m wind speeds. Though the
simulated wind speed ramp up for the Barstow location was slightly early on 3 July 2014, the observed strong winds persisted
longer over a similar time span before decaying. Accordingly, we can conclude that the model reproduced a realistic wind
evolution pattern over the Mojave Desert. While the actual dust conditions for the area are less clear, the lack of commentary
about dust in the recorded ASOS observer remarks leads us to believe that the simulated PM_{10} values for both the ALT3 and
ALT4 configurations in the Mojave Desert region were higher than what occurred. However, the cause of this discrepancy
is unclear. The erroneous PM_{10} feature could be due to issues with the drag partition treatment, unresolved sediment supply
influences, a combination of the two factors, or some other source of error within the model.

Though we are unable to do point-specific quantitative evaluations for the Phoenix metropolitan area due to the shifted
location of the main dust-producing outflow boundary in the simulations, we can see from our spatial PM_{10} time series analysis
(e.g., Fig. 12) that the maximum PM_{10} value during the peak of the dust event was generally co-located with the storm outflow
boundary. Thus, we compared the simulated maximum PM_{10} values for the area surrounding Phoenix with the maximum PM_{10}
values observed by the EPA stations as the dust wall passed over the city. Figure 13 shows time series of observed and simulated
maximum PM_{10} concentration for the combined Maricopa and Pinal counties in Arizona. This combined county area generally
encompasses the footprint of both the simulated and observed track of the storm. Note, the gust front in the simulation advanced
into the combined county area earlier than the recorded event (see Fig. 8), and the main dust wall moved away from the EPA
stations around Phoenix after 0300 UTC. Therefore, we expect the simulated combined county maximum PM_{10} values to be
higher than the observed PM_{10} conditions before and after the observed PM_{10} peak at 0200 UTC on 4 July 2014. During the
0000 UTC to 0300 UTC period, the observed maximum PM_{10} was was 9,132 μg m^{-3}, while the CTRL, ALT1, ALT3, and
ALT4 configurations produced maximum PM_{10} values for the combined county area of 17,151 μg m^{-3}, 419 μg m^{-3}, 8,539 μg
m^{-3}, and 7,240 μg m^{-3}, respectively. If we emphasize the order of magnitude over the exact value of PM_{10} from these results to
account for observed and simulated gust front location differences, both ALT3 and ALT4 produced reasonable results.

4   Discussion

Findings from this case study show that incorporating a drag partition treatment into the AFWA dust emission module can
improve simulated dust transport for vegetated dryland regions. The CTRL simulation results with no drag partitioning align
with previous findings that the default AFWA module settings produce excessive dust conditions in the southwest United States.
While the albedo-based drag partition method improved the results with respect to PM_{10} spatial patterns and concentration
magnitudes, we also achieved similar outcomes with a global wind scaling parameter.

We argue that the ALT4 globally scaled wind speed approach, at least how it's applied in our case study, should also
be considered a crude form of drag partitioning. However, unlike the Chappell and Webb (2016) method, this global drag

partitioning approach assumes that the effects of the variability in vegetation cover over the dust-producing areas within the model domain are relatively negligible to the dust entrainment process. Our case study results imply that the spatial variability of u_{ns*} was not a key factor in the evolution of the dust storm simulation, but this outcome may simply be an artifact of the conditions associated with our chosen case study. This particular dust event occurred in a confined, localized area due to its convective nature over a shrub-dominated landscape with relatively homogenous topography (e.g., Fig. 2-3). The spatial variability of u_{ns*} in the broader region may have more influence on dust events generated by synoptically driven wind forcing conditions (i.e., horizontal length scales on the order of several 100 to 1000+ km). Furthermore, the ALT4 configuration does not provide a viable modeling solution for users interested in exploring the effects of land management or land cover change on sediment transport and air quality and may be limited in its use to short term atmospheric forecasting applications.

It appears that drag partition treatments effectively suppressed the broadscale erroneous dust emissions in southern California and southwestern Arizona inherent to the CTRL configuration without restricting the dust emissions that generated the Phoenix haboob. However, the relatively low PM_{10} concentrations produced by the ALT1 simulation suggest that the S parameter was masking the absence of drag representation in the original AFWA code. Although the model performance for this case study is arguably better with the drag partition when $S = 1$, this may not be the case for all regions. Further investigation on the role of the S parameter in areas with more heterogeneous sediment supply is necessary to resolve this issue.

In order to better isolate the role of the u_{ns*} spatial heterogeneity in our results from the effects of soil moisture on the dust emission process, we reproduced the diagnostic excess friction speed time series from Fig. 10 but used the threshold friction speed for air-dry soil conditions for saltation size bin 7 instead of the moisture-corrected threshold value (u_{*ex_dry}; Fig. 15). The resultant u_{*ex_dry} values for all wind forcing treatments are, at least to some degree, largely higher in magnitude than their moisture-corrected counterparts in Fig. 10. However, both the u_{*ex} and u_{*ex_dry} values for the forested areas along the Mogollon Rim are generally low, even when using values for C_s that align with the albedo-derived u_{ns*} estimates associated with the barren and shrubland areas. For example, the u_{ns*} values for the forested Mogollon Rim region in Fig. 7 are primarily less than 0.02 throughout the peak of the dust event. This suggests model sensitivity for this domain to the albedo-based drag partition may vary for alternate wind flow conditions and that the albedo-based drag partition scheme could potentially benefit from additional validation studies.

We note, however, that modeled 10 m wind speeds will be reduced over forested areas due to the aerodynamic drag from the trees on simulated wind speeds and that these particular aerodynamic roughness effects vary as a function of the z_0 settings in the parent WRF model. The drag partition treatment, at least with respect to how it's configured in our modeling set up, has no influence on simulated winds outside of the dust emission calculation. Even if the u_{ns*} values were high for a model grid cell with forest cover, the simulated winds would likely be reduced by the internal WRF model physics, potentially mitigating (or masking) a shortfall in the drag partition correction.

These peculiar results over the forested area also highlight the need for consistency of aerodynamic roughness treatments between the dust emission module and other components of the parent weather model, including the land surface and planetary boundary layer schemes, so that u_* and u_{s*} diagnosed for the dust emission treatment are consistent with the other model elements governing simulated wind flow. Findings by Webb et al. (2014b) demonstrate how these kinds of inconsistencies can

lead to erroneously modeled increases in sediment transport with increasing vegetation coverage. As dust emission models like the AFWA module are further refined, careful consideration should be taken when configuring model components that incorporate land surface conditions on aerodynamic processes.

530   Even though we were able to largely replicate the PM_{10} case study simulations produced with the albedo-based drag partition by using a global scaling factor, it is important to remember that our C_s value selection was informed by the albedo-derived u_{ns*} values and that the relatively short duration of our case study event meant that the u_{ns*} values associated with our study were static throughout the event lifecycle. In any event, choosing an appropriate C_s value *a priori* could be challenging when using the globally scaled surface wind speed approach for operational forecasting or climatological applications or for a larger

535   domain with more variability in vegetation coverage over dust-producing areas.

    Spatial u_{ns*} patterns derived from MODIS data will likely evolve over longer time spans from processes like annual vegetation growth cycles, drought conditions, anomalous wet periods, and land cover change. To investigate, we reviewed the temporal coefficient of variation (CV) of 500 m gridded monthly mean snow-masked u_{ns*} values in our case study area over the 2001-2021 MODIS record (Fig. 16) and found that CV values generally ranged between 1-12% for grid pixels in the dust-

540   producing regions of southwest Arizona, with a few clusters of pixels ranging between 15-20% over active agricultural areas. By comparison, with the global C_s drag partitioning (ALT4), we saw markedly different spatial patterns in areas of the model domain capable of initiating saltation simply by varying the C_s parameter by increments of 0.005 (e.g., Fig. 10 and 15), or $C_s =$ $0.025 \pm \sim20\%$. Given that u_{ns*} and C_s are mathematically equivalent with respect to the model implementation (i.e., in terms of being multiplied by U_{10m} to generate u_{s*} in Eqs. 1 and 14, respectively), our MODIS-derived u_{ns*} CV analysis suggests

545   that $C_s = 0.025$ may be a reasonable setting for this domain in general. Nonetheless, though these CV values may appear to indicate a relatively low amount of variability in MODIS-derived u_{ns*} over the majority of the dust-producing region, even modest changes in u_{ns*} may result in simulated u_{s*} values exceeding or falling below u_{*ts}.

    Thus, the degree to which the observed variability in u_{ns*} matters from a mesoscale dust modeling context is still unclear. Okin (2005) explored the influence of surface heterogeneity on saltation flux following the original method of Raupach et al.

550   (1993), where the drag partition adjusts u_{*ts} directly rather than modifyng the u_* value driving the saltation flux equation. When reviewing the daily saltation flux as a function of the CV of u_{*ts}, Okin (2005) found that CV values of 10% or less produced minimal differences in saltation flux. Additional modeling case studies focused on seasonal and interannual land cover changes are needed to determine the sensitivity of the AFWA dust emission module to u_{ns*} variability.

    Based on these findings, we argue that the Chappell and Webb (2016) drag partition approach may have the potential to

555   improve dust transport model performance in vegetated dryland regions. Still, it is worth discussing the nuances associated with its use. On the one hand, the technique removes the dependence on greenness-related remote-sensing indicators. By using albedo in a way that is interpreted as shadow to discern roughness elements and their associated aerodynamic properties, the Chappell and Webb (2016) technique may capture the drag induced by plants as well as drag generated by engineered and natural structures like fences, tillage furrows, and subgrid-scale topographic relief. In theory, this method incorporates

560   subgrid-scale heterogeneity and temporal variability in its calculation.

Another aspect to consider is the use of 10 m wind speed in Eq. (1), which is not physically based. The original derivation for u_{s*} multiplied u_{ns*} by a parameter Chappell and Webb (2016) referred to as "the freestream wind speed" or U_f (also referred to by some studies as U_h). Yet this U_f parameter is not associated with wind speed in the free atmosphere (i.e., wind speed above the atmospheric boundary layer). Instead, the value stems from the freestream flow associated with the wind tunnel data collected by Marshall (1971) that Chappell and Webb (2016) used to develop their equations, which has no direct replacement. Additional research is needed to assess the degree of error introduced by the $U_f = U_{10m}$ assumption.

The Chappell and Webb (2016) scheme also assumes that all observed shadows emanate from solid subgrid-scale roughness objects within the flow field. This assumption could be obviated if shadows cast by tall objects extend into neighboring grid cells, creating a sensitivity to wind direction. While this is not likely to be an issue at the mesoscale or coarser modeling scales with u_{ns*} values derived from 500 m MODIS data, additional lower-bound grid resolution limitation studies may be necessary before applying the Chappell and Webb (2016) drag partition method to finer-scale dust transport models (e.g., large eddy simulation and field scale models) with u_{ns*} initialized from high-fidelity data sources.

Like many other parameterizations, the Chappell and Webb (2016) drag partition is empirical. It incorporates multiple rounds of normalization and draws conclusions about nature from idealized "black-sky" (i.e., 100% direct illumination) scenarios that do not exist in real-world settings. Furthermore, the Marshall (1971) wind tunnel experiments that Chappell and Webb (2016) used to establish their drag partition equations used non-porous, rigid cylinders to imitate natural roughness elements. Multiple studies have since demonstrated that the cylinder method is often a poor representation the aerodynamic behavior of live vegetation (e.g., Walter et al., 2012). Arguably, the effects of uncertainties in the rescaling parameters associated with the albedo approach on simulated dust entrainment outcomes may be comparable to errors created by uncertainties in inputs and configuration parameters required for other drag partition methods. Additional studies comparing the many available drag partitioning approaches in mesoscale and global scale dust transport models over extended periods of vegetation green-up and scenecence are needed to fully resolve this issue.

Given the relative simplicity of implementing the Chappell and Webb (2016) drag partition into dust emission modeling code, it would be worthwhile to continue investigating use of the scheme in convection-permitting and regional-scale dust transport models. At these scales, many of the aforementioned issues would likely be small or negligible compared to errors introduced by other parts of the modeling framework that govern u_* and erodible sediment supply. In fact, some U.S. agencies have already begun to incorporate the Chappell and Webb (2016) drag partition into their operational air quality models (e.g., Tong et al., 2020).

Finally, though the MODIS data preprocessing steps required by the Chappell and Webb (2016) drag partition are comparable to the processing requirements of other air quality and weather model input datasets, operational environmental prediction agencies may find the additional processing burden prohibitive. The computational resource allocations of production systems are often operating near capacity in order to meet a multitude of simulation parameter output requirements and data dissemination schedules, making it challenging to justify added data ingest and preprocessing steps for a single model parameter. Accordingly, future efforts could explore the feasibility of using monthly or seasonal climatologies of u_{ns*} for weather forecasting applications.

5 Conclusions

This study explored the use of an albedo-based drag partitioning scheme introduced by Chappell and Webb (2016) to incorporate roughness effects into a widely-used dust emission and transport model within WRF-Chem. Our results for a convective dust event case study for the desert region around Phoenix, Arizona support previous findings that the original WRF-Chem/GOCART/AFWA model configuration is prone to producing widespread erroneous dust emissions in the southwestern United States. Furthermore, our findings suggest that incorporating a drag partition treatment into the AFWA dust emission module may improve dust transport simulation and forecasting in vegetated dryland regions through better sheltering-effect representation on dust emissions. This code adaptation could take the form of a formal drag partition treatment or a wind speed-tuning approach if the roughness element coverage of the dust-producing areas associated with the model domain is somewhat homogenous and the simulation is run over a short enough period that the surface roughness configuration does not change. We note, however, that we cannot generalize model performance from a single case study event. Instead, we view this study as a preliminary demonstration of capability and motivation to further explore the use of drag partitioning in dust transport models to account for roughness effects on the dust entrainment process. Additional case studies and seasonal analyses are necessary to determine if the Chappell and Webb (2016) drag partition method can reliably improve dust simulations used for various weather prediction, land management, and climate change modeling applications.

The benefits of using a drag partition methodology in the AFWA module are manifest in the vast improvements we see with ALT3 and ALT4 over the initial CTRL configuration. Follow on studies are still necessary to explore if these benefits persist over longer simulation periods. However, we anticipate that satellite-derived roughness information could markedly improve investigations of the role of short- and long-term changes in vegetation on dust emission patterns. This, in turn, could be of benefit to model users interested in drought hazard, climate change, land management, land use/land cover change, and post-wild fire condition modeling applications.

Code availability. WRF-Chem v4.1 baseline source code and run instructions are available for download at https://github.com/wrf-model/WRF/releases/tag/v4.1 (last access: 1 June 2020). The modified version of WRF-Chem v4.1 used to produce the results described in this paper is available for download via Zenodo (https://doi.org/10.5281/zenodo.7447886, Letcher et al., 2022). This modified source code includes additional run time-activated functions that allow users to easily switch between the original AFWA dust emission module settings (i.e., CTRL) and the alternate configurations with drag partition included (i.e., ALT1, ALT2, ALT3, and ALT4). The Zenodo repository also includes a copy of the WRF Pre-processing System v4.2 code used to prepare the terrain and forcing data for our case study simulations. Detailed modified code descriptions, guidance for preparing the MODIS u_{ns*} input data, and model run-time instructions are thoroughly documented in the report by Michaels et al. (2022).

Appendix A: Variable list

Tables A1-A3 provide the symbol, name, units, and value or description of variables referred to throughout this paper. Values of prescribed constants are listed. Variable arrays are described as "variable" for size bin-related settings, "spatially varying parameter" for static fields, and "spatiotemporally varying parameter" for temporally dynamic fields. See Fig. 6 for a schematic overview of how these parameters are used in the AFWA module calculations.

Author contributions. SLLeG developed the project concept and experimental design, performed the majority of the data analysis and interpretation, served as the primary manuscript author, and led project efforts. SD provided the MODIS-derived u_{ns*} input datasets. TWL modified the WRF-Chem code to implement the albedo drag partition into the AFWA module and produced the WRF-Chem case study simulation data. ARG, SLLeG, TSH, and TWL conducted the gust front location offsest assessment. SD performed the u_{ns*} CV analysis. GSO, NPW, and SLLeG collaboratively revised analyses and interpretation. All co-authors critically reviewed the manuscript.

Competing interests. The authors declare that they have no conflict of interest.

Acknowledgements. Funding support for this research was provided by the U.S. Army Engineer Research and Development Center (ERDC) Extreme Terrain Research Program, "Forecasting EO/IR Extinction Characteristics for Active and Passive Optical Systems" project under Work Item H407HL, Funding Account Number U4365035 sponsored by the Assistant Secretary of the Army for Acquisition, Logistics, and Technology (ASA-ALT). NPW and SD were supported by NASA ROSES grant no. 80NSSC20K1673. Contributions by GSO were supported by NIH grant no. R01AI148336. Any use of trade, product, or firm names is for descriptive purposes only and does not imply endorsement by the U.S. Government. Permission to publish was granted by the ERDC Geospatial Research Laboratory. The USDA is an equal opportunity provider and employer.

References

Adams, D. K. and Comrie, A. C.: The North American Monsoon, Bull. Am. Meteorol. Soc., 78, 2197–2213, https://doi.org/10.1175/1520-0477(1997)078<2197:TNAM>2.0.CO;2, 1997.

Aragnou, E., Watt, S., Duc, H. N., Cheeseman, C., Riley, M., Leys, J., White, S., Salter, D., Azzi, M., Chang, L. T.-C., Morgan, G., and Hannigan, I.: Dust transport from inland Australia and its impact on air quality and health on the eastern coast of Australia during the February 2019 dust storm, Atmosphere, 12, 141, https://doi.org/10.3390/atmos12020141, 2021.

Asadov, Kh. G. and Kerimov, N. I.: On the necessity of correction of the methodology for calculating aerosol flux from the Earth's surface to the atmosphere using the NDVI index, Fundamental and Applied Climatology, 3, 92–101, https://doi.org/10.21513/2410-8758-2019-3-92-101, 2019. [In Russian]

Barnard, J. C., Fast, J. D., Paredes-Miranda, G., Arnott, W. P., and Laskin, A.: Technical Note: Evaluation of the WRF-Chem "Aerosol Chemical to Aerosol Optical Properties" Module using data from the MILAGRO campaign, Atmos. Chem. Phys., 10, 7325–7340, https://doi.org/10.5194/acp-10-7325-2010, 2010.

Benjamin, S. G., Weygandt, S. S., Brown, J. M., Hu, M., Alexander, C. R., Smirnova, T. G., Olson, J. B., James, E. P., Dowell, D. C., Grell, G. A., Lin, H., Peckham, S. E., Smith, T. L., Moninger, W. R., Kenyon, J. S., and Manikin, G. S.: A North American hourly assimilation and model forecast cycle: The Rapid Refresh, Mon. Weather Rev., 144, 1669–1694, https://doi.org/10.1175/MWR-D-15-0242.1, 2016.

Brown, S., Nickling, W. G., and Gillies, J. A.: A wind tunnel examination of shear stress partitioning for an assortment of surface roughness distributions, J. Geophys. Res., 113, https://doi.org/10.1029/2007JF000790, 2008.

Bukowski, J. and van den Heever, S. C.: The impact of land surface properties on haboobs and dust lofting, J. Atmos. Sci., 79, 3195–3218, https://doi.org/10.1175/JAS-D-22-0001.1, 2022.

Cakmur, R. V., Miller, R. L., Perlwitz, J., Geogdzhayev, I. V., Ginoux, P., Koch, D., Kohfeld, K. E., Tegen, I., and Zender, C. S.: Constraining the magnitude of the global dust cycle by minimizing the difference between a model and observations, J. Geophys. Res., 111, D06207, https://doi.org/10.1029/2005JD005791, 2006.

Chappell, A., Van Pelt, S., Zobeck, T., and Dong, Z.: Estimating aerodynamic resistance of rough surfaces using angular reflectance, Remote Sens. Environ., 114, 1462–1470, https://doi.org/10.1016/j.rse.2010.01.025, 2010.

Chappell, A. and Webb, N. P.: Using albedo to reform wind erosion modelling, mapping and monitoring, Aeolian Res., 23, 63–78, https://doi.org/10.1016/j.aeolia.2016.09.006, 2016.

Chin, M., Rood, R. B., Lin, S.-J., Müller, J.-F., and Thompson, A. M.: Atmospheric sulfur cycle simulated in the global model GOCART: Model description and global properties, J. Geophys. Res.-Atmos., 105, 24,671-24,687, https://doi.org/10.1029/2000JD900384, 2000.

Collins, W. J., Bellouin, N., Doutriaux-Boucher, M., Gedney, N., Halloran, P., Hinton, T., Hughes, J., Jones, C. D., Joshi, M., Liddicoat, S., Martin, G., O'Connor, F., Rae, J., Senior, C., Sitch, S., Totterdell, I., Wiltshire, A., and Woodward, S.: Development and evaluation of an Earth-system model – HadGEM2, Geosci. Model Dev., 4, 1051–1075, https://doi.org/10.5194/gmd-4-1051-2011, 2011.

Cremades, P. G., Fernández, R. P., Allende, D. G., Mulena, G. C., and Puliafito, S. E.: High resolution satellite derived erodibility factors for WRF/Chem windblown dust simulations in Argentina, Atmósfera, 30, 11–25, https://doi.org/10.20937/ATM.2017.30.01.02, 2017.

Darmenova, K., Sokolik, I. N., Shao, Y., Marticorena, B., and Bergametti, G.: Development of a physically based dust emission module within the Weather Research and Forecasting (WRF) model: Assessment of dust emission parameterizations and input parameters for source regions in Central and East Asia, J. Geophys. Res., 114, https://doi.org/10.1029/2008JD011236, 2009.

Ek, M. B., Mitchell, K. E., Lin, Y., Rogers, E., Grunmann, P., Koren, V., Gayno, G., and Tarpley, J. D.: Implementation of Noah land surface

680   model advances in the National Centers for Environmental Prediction operational mesoscale Eta model, J. Geophys. Res.-Atmos., 108, https://doi.org/10.1029/2002JD003296, 2003.

Evans, S., Ginoux, P., Malyshev, S., and Shevliakova, E.: Climate-vegetation interaction and amplification of Australian dust variability, Geophys. Res. Lett., 43, https://doi.org/10.1002/2016GL071016, 2016.

Fast, J. D., Gustafson, W. I., Easter, R. C., Zaveri, R. A., Barnard, J. C., Chapman, E. G., Grell, G. A., and Peckham, S. E.: Evolution of

685   ozone, particulates, and aerosol direct radiative forcing in the vicinity of Houston using a fully coupled meteorology-chemistry-aerosol model, J. Geophys. Res., 111, https://doi.org/10.1029/2005JD006721, 2006.

Fécan, F., Marticorena, B., and Bergametti, G.: Parametrization of the increase of the aeolian erosion threshold wind friction velocity due to soil moisture for arid and semi-arid areas, 17, 149–157, https://doi.org/10.1007/s00585-999-0149-7, 1999.

Francis, D., Nelli, N., Fonseca, R., Weston, M., Flamant, C., and Cherif, C.: The dust load and radiative impact associated with the June 2020

690   historical Saharan dust storm, Atmos. Environ., 268, 118808, https://doi.org/10.1016/j.atmosenv.2021.118808, 2022.

Fountoukis, C., Ackermann, L., Ayoub, M. A., Gladich, I., Hoehn, R. D., and Skillern, A.: Impact of atmospheric dust emission schemes on dust production and concentration over the Arabian Peninsula, Model. Earth Syst. Environ., 2, https://doi.org/10.1007/s40808-016-0181-z, 2016.

Freitas, S. R., Longo, K. M., Alonso, M. F., Pirre, M., Marecal, V., Grell, G., Stockler, R., Mello, R. F., and Sánchez Gácita, M.: PREP-

695   CHEM-SRC – 1.0: a preprocessor of trace gas and aerosol emission fields for regional and global atmospheric chemistry models, Geosci. Model Dev., 4, 419–433, https://doi.org/10.5194/gmd-4-419-2011, 2011.

Fu, L.-T.: Comparisons suggest more efforts are required to parameterize wind flow around shrub vegetation elements for predicting aeolian flux, Sci. Rep., 9, https://doi.org/10.1038/s41598-019-40491-z, 2019.

Gallagher, A. R., LeGrand, S. L., Hodgdon, T. S., and Letcher, T. W.: Simulating environmental conditions for southwest United States

700   convective dust storms using the Weather Research and Forecasting model v4.1, ERDC TR-22-11, U.S. Army Engineer Research and Development Center, Hanover, New Hampshire, USA, https://doi.org//10.21079/11681/44963, 2022.

Gillette, D. A.: Fine particulate emissions due to wind erosion, Trans. ASAE, 20, 0890–0897, https://doi.org/10.13031/2013.35670, 1977.

Gillette, D. A., Herrick, J. E., and Herbert, G. A.: Wind characteristics of mesquite streets in the Northern Chihuahuan Desert, New Mexico, USA, Environ. Fluid Mech., 6, 241–275, https://doi.org/10.1007/s10652-005-6022-7, 2006.

705 Ginoux, P., Chin, M., Tegen, I., Prospero, J. M., Holben, B., Dubovik, O., and Lin, S.-J.: Sources and distributions of dust aerosols simulated with the GOCART model, J. Geophys. Res., 106, 20255–20273, https://doi.org/10.1029/2000JD000053, 2001.

Gong, S. L.: A parameterization of sea-salt aerosol source function for sub- and super-micron particles, Glob. Biogeochem. Cycles, 17, 1097, https://doi.org/10.1029/2003GB002079, 2003.

Grell, G. A., Peckham, S. E., Schmitz, R., McKeen, S. A., Frost, G., Skamarock, W. C., and Eder, B.: Fully coupled "online" chemistry

710   within the WRF model, Atmos. Environ., 39, 6957–6975, https://doi.org/10.1016/j.atmosenv.2005.04.027, 2005.

Hamzeh, N. H., Karami, S., Kaskaoutis, D. G., Tegen, I., Moradi, M., and Opp, C.: Atmospheric dynamics and numerical simulations of six frontal dust storms in the Middle East region, Atmosphere, 12, 125, https://doi.org/10.3390/atmos12010125, 2021.

Han, J. and Pan, H.-L.: Revision of convection and vertical diffusion schemes in the NCEP Global Forecast System, Weather Forecast., 26, 520–533, https://doi.org/10.1175/WAF-D-10-05038.1, 2011.

715 Hyde, P., Mahalov, A., and Li, J.: Simulating the meteorology and PM$_{10}$ concentrations in Arizona dust storms using the Weather Research and Forecasting model with Chemistry (Wrf-Chem), J. Air Waste Manag., 68, 177–195, https://doi.org/10.1080/10962247.2017.1357662, 2018.

Iacono, M. J., Delamere, J. S., Mlawer, E. J., Shephard, M. W., Clough, S. A., and Collins, W. D.: Radiative forcing by long-lived greenhouse gases: Calculations with the AER radiative transfer models, J. Geophys. Res., 113, https://doi.org/10.1029/2008JD009944, 2008.

720 Ito, A. and Kok, J. F.: Do dust emissions from sparsely vegetated regions dominate atmospheric iron supply to the Southern Ocean?, J. Geophys. Res.-Atmos., 122, 3987–4002, https://doi.org/10.1002/2016JD025939, 2017.

Karumuri, R. K., Kunchala, R. K., Attada, R., Dasari, H. P., and Hoteit, I.: Seasonal simulations of summer aerosol optical depth over the Arabian Peninsula using WRF-Chem: Validation, climatology, and variability, Int. J. Climatol., 42, 2901–2922, https://doi.org/10.1002/joc.7396, 2022.

725 Kim, D., Chin, M., Bian, H., Tan, Q., Brown, M. E., Zheng, T., You, R., Diehl, T., Ginoux, P., and Kucsera, T.: The effect of the dynamic surface bareness on dust source function, emission, and distribution, J. Geophys. Res.-Atmos., 118, 871–886, https://doi.org/10.1029/2012JD017907, 2013.

Kim, K., Kim, S., Choi, M., Kim, M., Kim, J., Shin, I., Kim, J., Chung, C., Yeo, H., Kim, S., Joo, S. J., McKeen, S. A., and Zhang, L.: Modeling Asian dust storms using WRF-Chem during the DRAGON-Asia Field Campaign in April 2012, J. Geophys. Res.-Atmos., 126, 730 https://doi.org/10.1029/2021JD034793, 2021.

King, J., Nickling, W. G., and Gillies, J. A.: Representation of vegetation and other nonerodible elements in aeolian shear stress partitioning models for predicting transport threshold, J. Geophys. Res. Earth Surf., 110, https://doi.org/10.1029/2004JF000281, 2005.

Kok, J. F.: A scaling theory for the size distribution of emitted dust aerosols suggests climate models underestimate the size of the global dust cycle, Proc. Natl. Acad. Sci., 108, 1016–1021, https://doi.org/10.1073/pnas.1014798108, 2011.

735 Kok, J. F., Parteli, E. J. R., Michaels, T. I., and Karam, D. B.: The physics of wind-blown sand and dust, Rep. Prog. Phys., 75, 106901, https://doi.org/10.1088/0034-4885/75/10/106901, 2012.

Kok, J. F., Albani, S., Mahowald, N. M., and Ward, D. S.: An improved dust emission model – Part 2: Evaluation in the Community Earth System Model, with implications for the use of dust source functions, Atmos. Chem. Phys., 14, 13043–13061, https://doi.org/10.5194/acp-14-13043-2014, 2014.

740 Koven, C. D. and Fung, I.: Identifying global dust source areas using high-resolution land surface form, J. Geophys. Res., 113, https://doi.org/10.1029/2008JD010195, 2008.

Kuchera, E. L., Rentschler, S. A., Creighton, G. A., and Rugg, S. A.: A review of operational ensemble forecasting efforts in the United States Air Force, Atmosphere, 12, 677, https://doi.org/10.3390/atmos12060677, 2021.

LeGrand, S. L., Polashenski, C., Letcher, T. W., Creighton, G. A., Peckham, S. E., and Cetola, J. D.: The AFWA dust emission scheme for 745 the GOCART aerosol model in WRF-Chem v3.8.1, Geosci. Model Dev., 12, 131–166, https://doi.org/10.5194/gmd-12-131-2019, 2019.

Letcher, T. W. and LeGrand, S. L.: A comparison of simulated dust produced by three dust-emission schemes in WRF-Chem: Case study assessment, ERDC/CRREL TR-18-13, U.S. Army Engineer Research and Development Center, Hanover, New Hampshire, USA, https://doi.org/10.21079/11681/28868, 2018.

Letcher, T. W., LeGrand, S. L., and Michaels, M. L.: WRF-Chem-v4.1-AFWA-Drag-Partition-Modifications: Full model code release (bug-750 fix release) (v1.1.1), Zenodo [code], https://doi.org/10.5281/zenodo.7447886, 2022.

Li, J., Okin, G. S., Herrick, J. E., Belnap, J., Miller, M. E., Vest, K., and Draut, A. E.: Evaluation of a new model of aeolian transport in the presence of vegetation, J. Geophys. Res. Earth Surf., 118, 288–306, https://doi.org/10.1002/jgrf.20040, 2013.

Ma, S., Zhang, X., Gao, C., Tong, D. Q., Xiu, A., Wu, G., Cao, X., Huang, L., Zhao, H., Zhang, S., Ibarra-Espinosa, S., Wang, X., Li, X., and Dan, M.: Multimodel simulations of a springtime dust storm over northeastern China: implications of an evaluation of four commonly used air quality models (CMAQ v5.2.1, CAMx v6.50, CHIMERE v2017r4, and WRF-Chem v3.9.1), Geosci. Model Dev., 12, 4603–4625, https://doi.org/10.5194/gmd-12-4603-2019, 2019.

Marshall, J. K.: Drag measurements in roughness arrays of varying density and distribution, Agric. Meteorol., 8, 269–292, https://doi.org/10.1016/0002-1571(71)90116-6, 1971.

Marticorena, B. and Bergametti, G.: Modeling the atmospheric dust cycle: 1. Design of a soil-derived dust emission scheme, J. Geophys. Res., 100, 16415, https://doi.org/10.1029/95JD00690, 1995.

Marticorena, B., Bergametti, G., Aumont, B., Callot, Y., N'Doumé, C., and Legrand, M.: Modeling the atmospheric dust cycle: 2. Simulation of Saharan dust sources, J. Geophys. Res.-Atmos., 102, 4387–4404, https://doi.org/10.1029/96JD02964, 1997.

Mayaud, J. and Webb, N.: Vegetation in drylands: Effects on wind flow and aeolian sediment transport, 6, 64, https://doi.org/10.3390/land6030064, 2017.

Mesbahzadeh, T., Salajeghe, A., Sardoo, F. S., Zehtabian, G., Ranjbar, A., Marcello Miglietta, M., Karami, S., and Krakauer, N. Y.: Spatial-temporal variation characteristics of vertical dust flux simulated by WRF-Chem model with GOCART and AFWA dust emission schemes (Case study: Central Plateau of Iran), Appl. Sci., 10, 4536, https://doi.org/10.3390/app10134536, 2020.

Michaels, M. L., Letcher, T. W., LeGrand, S. L., Webb, N. P., and Putnam, J. B.: Implementation of an albedo-based drag partition into the WRF-Chem v4.1 AFWA dust emission module, ERDC/CRREL TR-22-2, U.S. Army Engineer Research and Development Center, Hanover, New Hampshire, USA, https://doi.org/10.21079/11681/42782, 2022.

Miller, P. W., Williams, M., and Mote, T.: Modeled atmospheric optical and thermodynamic responses to an exceptional Trans-Atlantic dust outbreak, J. Geophys. Res.-Atmos., 126, e2020JD032909, https://doi.org/10.1029/2020JD032909, 2021.

Mohebbi, A., Green, G. T., Akbariyeh, S., Yu, F., Russo, B. J., and Smaglik, E. J.: Development of dust storm modeling for use in freeway safety and operations management: An Arizona case study, Transp. Res. Rec. J. Transp. Res. Board, 2673, 175–187, https://doi.org/10.1177/0361198119839978, 2019.

Mohebbi, A., Yu, F., Cai, S., Akbariyeh, S., and Smaglik, E. J.: Spatial study of particulate matter distribution, based on climatic indicators during major dust storms in the State of Arizona, Front. Earth Sci., 15, 133–150, https://doi.org/10.1007/s11707-020-0814-4, 2020.

Nabavi, S. O., Haimberger, L., and Samimi, C.: Sensitivity of WRF-chem predictions to dust source function specification in West Asia, Aeolian Res., 24, 115–131, https://doi.org/10.1016/j.aeolia.2016.12.005, 2017.

Nakanishi, M. and Niino, H.: An improved Mellor–Yamada Level-3 Model with condensation physics: Its design and verification, Boundary Layer Meteorol., 112, 1–31, https://doi.org/10.1023/B:BOUN.0000020164.04146.98, 2004.

Nguyen, H. D., Riley, M., Leys, J., and Salter, D.: Dust storm event of February 2019 in Central and East Coast of Australia and evidence of long-range transport to New Zealand and Antarctica, 10, 653, https://doi.org/10.3390/atmos10110653, 2019.

Nikfal, A., Raadatabadi, A., and Sehatkashani, S.: Investigation of dust schemes in the model WRF/Chem. J. Air Pollut. Health, 3, 1-8, 2018.

Okin, G. S.: Dependence of wind erosion and dust emission on surface heterogeneity: Stochastic modeling, J. Geophys. Res., 110, D11208, https://doi.org/10.1029/2004JD005288, 2005.

Okin, G. S.: A new model of wind erosion in the presence of vegetation, J. Geophys. Res., 113, F02S10, https://doi.org/10.1029/2007JF000758, 2008.

Okin, G. S.: The contribution of brown vegetation to vegetation dynamics, 91, 743–755, https://doi.org/10.1890/09-0302.1, 2010.

790 Parajuli, S. P. and Zender, C. S.: Projected changes in dust emissions and regional air quality due to the shrinking Salton Sea, Aeolian Res., 33, 82–92, https://doi.org/10.1016/j.aeolia.2018.05.004, 2018.

Parajuli, S. P., Stenchikov, G. L., Ukhov, A., and Kim, H.: Dust emission modeling using a new high-resolution dust source function in WRF-Chem with implications for air quality, J. Geophys. Res.-Atmos., 124, 10,109–10,133, https://doi.org/10.1029/2019JD030248, 2019.

Parajuli, S. P., Stenchikov, G. L., Ukhov, A., Shevchenko, I., Dubovik, O., and Lopatin, A.: Aerosol vertical distribution and interactions with
795 land/sea breezes over the eastern coast of the Red Sea from lidar data and high-resolution WRF-Chem simulations, Atmos. Chem. Phys., 20, 16,089–16,116, https://doi.org/10.5194/acp-20-16089-2020, 2020.

Peckham, S. E., Grell, G., McKeen, S. A., Ahmadov, R., Wong, K. Y., Barth, M., Pfister, G., Wiedinmyer, C., Fast, J. D., Gustafson, W. I., Ghan, S. J., Zaveri, R., Easter, R. C., Barnard, J., Chapman, E., Hewson, M., Schmitz, R., Salzmann, M., Beck, V., and Freitas, S. R.: WRF-Chem version 3.8.1 user's guide, https://doi.org/10.7289/V5/TM-OAR-GSD-48, 2017.

800 Péré, J.-C., Rivellini, L., Crumeyrolle, S., Chiapello, I., Minvielle, F., Thieuleux, F., Choël, M., and Popovici, I.: Simulation of African dust properties and radiative effects during the 2015 SHADOW campaign in Senegal, Atmos. Res., 199, 14–28, https://doi.org/10.1016/j.atmosres.2017.07.027, 2018.

Pierre, C., Bergametti, G., Marticorena, B., Kergoat, L., Mougin, E., and Hiernaux, P.: Comparing drag partition schemes over a herbaceous Sahelian rangeland: Drag partitions comparison in Sahel, J. Geophys. Res. Earth Surf., 119, 2291–2313,
805 https://doi.org/10.1002/2014JF003177, 2014.

Raupach, M. and Lu, H.: Representation of land-surface processes in aeolian transport models, Environ. Modell. Softw., 19, 93–112, https://doi.org/10.1016/S1364-8152(03)00113-0, 2004.

Raupach, M. R.: Drag and drag partition on rough surfaces, Boundary Layer Meteorol., 60, 375–395, https://doi.org/10.1007/BF00155203, 1992.

810 Raupach, M. R., Gillette, D. A., and Leys, J. F.: The effect of roughness elements on wind erosion threshold, J. Geophys. Res.-Atmos., 98, 3023–3029, https://doi.org/10.1029/92JD01922, 1993.

Rizza, U., Anabor, V., Mangia, C., Miglietta, M. M., Degrazia, G. A., and Passerini, G.: WRF-Chem simulation of a Saharan dust out-breakover the Mediterranean regions, Ciência e Natura, 38, 330, https://doi.org/10.5902/2179460X20249, 2016.

Rizza, U., Kandler, K., Eknayan, M., Passerini, G., Mancinelli, E., Virgili, S., Morichetti, M., Nolle, M., Eleftheriadis, K., Vasilatou, V.,
815 and Ielpo, P.: Investigation of an intense dust outbreak in the Mediterranean using XMed-Dry Network, multiplatform observations, and numerical modeling, Appl. Sci., 11, 1566, https://doi.org/10.3390/app11041566, 2021

Saidou Chaibou, A. A., Ma, X., Kumar, K. R., Jia, H., Tang, Y., and Sha, T.: Evaluation of dust extinction and vertical pro-files simulated by WRF-Chem with CALIPSO and AERONET over North Africa, J. Atmos. Sol.-Terr. Phys., 199, 105213, https://doi.org/10.1016/j.jastp.2020.105213, 2020.

820 Saleeby, S. M., van den Heever, S. C., Bukowski, J., Walker, A. L., Solbrig, J. E., Atwood, S. A., Bian, Q., Kreidenweis, S. M., Wang, Y., Wang, J., and Miller, S. D.: The influence of simulated surface dust lofting and atmospheric loading on radiative forcing, Atmos. Chem. Phys., 19, 10279–10301, https://doi.org/10.5194/acp-19-10279-2019, 2019.

Shao, Y., Nickling, W., Bergametti, G., Butler, H., Chappell, A., Findlater, P., Gillies, J., Ishizuka, M., Klose, M., Kok, J. F., Leys, J., Lu, H., Marticorena, B., McTainsh, G., McKenna-Neuman, C., Okin, G. S., Strong, C., and Webb, N.: A tribute to Michael R. Raupach for
825 contributions to aeolian fluid dynamics, Aeolian Res., 19, 37–54, https://doi.org/10.1016/j.aeolia.2015.09.004, 2015.

Skamarock, W. C., Klemp, J. B., Dudhia, J., Gill, D. O., Liu, Z., Berner, J., Wang, W., Powers, J. G., Duda, M. G., Barker, D. M., and Huang, X.-Y.: A description of the Advanced Research WRF Model version 4, UCAR/NCAR, https://doi.org/10.5065/1DFH-6P97, 2019.

Solomos, S., Kalivitis, N., Mihalopoulos, N., Amiridis, V., Kouvarakis, G., Gkikas, A., Binietoglou, I., Tsekeri, A., Kazadzis, S., Kottas, M., Pradhan, Y., Proestakis, E., Nastos, P., and Marenco, F.: From tropospheric folding to Khamsin and Foehn winds: How atmospheric
830   dynamics advanced a record-breaking dust episode in Crete, 9, 240, https://doi.org/10.3390/atmos9070240, 2018.

Solomos, S., Abuelgasim, A., Spyrou, C., Binietoglou, I., and Nickovic, S.: Development of a dynamic dust source map for NMME-DREAM v1.0 model based on MODIS Normalized Difference Vegetation Index (NDVI) over the Arabian Peninsula, Geosci. Model Dev., 12, 979–988, https://doi.org/10.5194/gmd-12-979-2019, 2019.

Spyrou, C., Solomos, S., Bartsotas, N. S., Douvis, K. C., and Nickovic, S.: Development of a dust source map for WRF-Chem model based
835   on MODIS NDVI, Atmosphere, 13, 868, https://doi.org/10.3390/atmos13060868, 2022.

Stull, R. B. (Ed.): An Introduction to Boundary Layer Meteorology, Springer Netherlands, Dordrecht, https://doi.org/10.1007/978-94-009-3027-8, 1988.

Su, L. and Fung, J. C. H.: Sensitivities of WRF-Chem to dust emission schemes and land surface properties in simulating dust cycles during springtime over East Asia, J. Geophys. Res.-Atmos., 120, 11,215-11,230, https://doi.org/10.1002/2015JD023446, 2015.

840   Tegen, I., Harrison, S. P., Kohfeld, K., Prentice, I. C., Coe, M., and Heimann, M.: Impact of vegetation and preferential source areas on global dust aerosol: Results from a model study, J. Geophys. Res.-Atmos., 107, AAC 14, https://doi.org/10.1029/2001JD000963, 2002.

Teixeira, J. C., Carvalho, A. C., Tuccella, P., Curci, G., and Rocha, A.: WRF-chem sensitivity to vertical resolution during a saharan dust event, Phys. Chem. Earth Parts ABC, 94, 188–195, https://doi.org/10.1016/j.pce.2015.04.002, 2016.

Thompson, G., Field, P. R., Rasmussen, R. M., and Hall, W. D.: Explicit forecasts of winter precipitation using an im-
845   proved bulk microphysics scheme. Part II: Implementation of a new snow parameterization, Mon. Wea. Rev., 136, 5095–5115, https://doi.org/10.1175/2008MWR2387.1, 2008.

Tong, D., Lee, P., Tang, Y., Baker, B., Campbell, P.C., Saylor, R., Chai, T., Lamsal, L.N., Krotkov, N.A., Li, C. and Kondragunta, S.: "Advancing National Air Quality Forecasts through Emission Data Assimilation." 100th American Meteorological Society Annual Meeting. AMS, 2020.

850   Tsarpalis, K., Papadopoulos, A., Mihalopoulos, N., Spyrou, C., Michaelides, S., and Katsafados, P.: The implementation of a mineral dust wet deposition scheme in the GOCART-AFWA module of the WRF model, Remote Sens., 10, 1595, https://doi.org/10.3390/rs10101595, 2018.

Tsarpalis, K., Katsafados, P., Papadopoulos, A., and Mihalopoulos, N.: Assessing desert dust indirect effects on cloud microphysics through a cloud nucleation scheme: A case study over the Western Mediterranean, Remote Sens., 12, 3473, https://doi.org/10.3390/rs12213473,
855   2020.

Uzan, L., Egert, S., and Alpert, P.: Ceilometer evaluation of the eastern Mediterranean summer boundary layer height – first study of two Israeli sites, Atmos. Meas. Tech., 9, 4387–4398, https://doi.org/10.5194/amt-9-4387-2016, 2016.

Vukovic, A., Vujadinovic, M., Pejanovic, G., Andric, J., Kumjian, M. R., Djurdjevic, V., Dacic, M., Prasad, A. K., El-Askary, H. M., Paris, B. C., Petkovic, S., Nickovic, S., and Sprigg, W. A.: Numerical simulation of "an American haboob," Atmos. Chem. Phys., 14, 3211–3230,
860   https://doi.org/10.5194/acp-14-3211-2014, 2014.

Walker, A. L., Liu, M., Miller, S. D., Richardson, K. A., and Westphal, D. L.: Development of a dust source database for mesoscale forecasting in southwest Asia, J. Geophys. Res., 114, https://doi.org/10.1029/2008JD011541, 2009.

Walter, B., Gromke, C., and Lehning, M.: Shear-stress partitioning in live plant canopies and modifications to Raupach's model, Boundary-Layer Meteorol., 144, 217–241, https://doi.org/10.1007/s10546-012-9719-4, 2012.

865   Webb, N. P. and Pierre, C.: Quantifying anthropogenic dust emissions, 6, 286–295, https://doi.org/10.1002/2017EF000766, 2018.

Webb, N. P., Herrick, J. E., and Duniway, M. C.: Ecological site-based assessments of wind and water erosion: informing accelerated soil erosion management in rangelands, Ecol. Appl, 24, 1405–1420, https://doi.org/10.1890/13-1175.1, 2014a.

Webb, N. P., Okin, G. S., and Brown, S.: The effect of roughness elements on wind erosion: The importance of surface shear stress distribution, J. Geophys. Res.-Atmos., 119, 6066–6084, https://doi.org/10.1002/2014JD021491, 2014b.

870   Webb, N. P., Chappell, A., LeGrand, S. L., Ziegler, N. P., and Edwards, B. L.: A note on the use of drag partition in aeolian transport models, Aeolian Res., 42, 100560, https://doi.org/10.1016/j.aeolia.2019.100560, 2020.

Woodward, S.: Modeling the atmospheric life cycle and radiative impact of mineral dust in the Hadley Centre climate model, J. Geophys. Res.-Atmos., 106, 18,155–18,166, https://doi.org/10.1029/2000JD900795, 2001.

World Meteorological Organization (WMO): Manual on Codes: Part A - Alphanumeric Codes, Secretariat of the World Meteorological Organization, Geneva, Switzerland, https://www.wmo.int/pages/prog/www/WMOCodes/WMO306_vI1/Publications/2018update/WMO306_vI1_2011UP2018_en.pdf, 2018.

Xu, X., Wang, J., Wang, Y., Henze, D. K., Zhang, L., Grell, G. A., McKeen, S. A., and Wielicki, B. A.: Sense size-dependent dust loading and emission from space using reflected solar and infrared spectral measurements: An observation system simulation experiment, J. Geophys. Res.-Atmos., 122, 8233–8254, https://doi.org/10.1002/2017JD026677, 2017.

880   Yu, M. and Yang, C.: Improving the non-hydrostatic numerical dust model by integrating soil moisture and greenness vegetation fraction data with different spatiotemporal resolutions, 11, e0165616, https://doi.org/10.1371/journal.pone.0165616, 2016.

Yu, M., Wu, B., Yan, N., Xing, Q., and Zhu, W.: A method for estimating the aerodynamic roughness length with NDVI and BRDF signatures using multi-temporal Proba-V data, Remote Sens., 9, 6, https://doi.org/10.3390/rs9010006, 2016.

Yuan, T., Chen, S., Huang, J., Zhang, X., Luo, Y., Ma, X., and Zhang, G.: Sensitivity of simulating a dust storm over Central Asia to different dust schemes using the WRF-Chem model, Atmos. Environ., 207, 16–29, https://doi.org/10.1016/j.atmosenv.2019.03.014, 2019.

885   Zhang, L., Grell, G. A., McKeen, S. A., Ahmadov, R., Froyd, K. D., and Murphy, D.: Inline coupling of simple and complex chemistry modules within the global weather forecast model FIM (FIM-Chem v1), Geosci. Model Dev., 15, 467–491, https://doi.org/10.5194/gmd-15-467-2022, 2022.

Zhao, J., Ma, X., Wu, S., and Sha, T.: Dust emission and transport in Northwest China: WRF-Chem simulation and comparisons with multi-sensor observations, Atmos. Res., 241, 104978, https://doi.org/10.1016/j.atmosres.2020.104978, 2020.

890   Zhou, M., Zhang, L., Chen, D., Gu, Y., Fu, T.-M., Gao, M., Zhao, Y., Lu, X., and Zhao, B.: The impact of aerosol–radiation interactions on the effectiveness of emission control measures, Environ. Res. Lett., 14, 024002, https://doi.org/10.1088/1748-9326/aaf27d, 2019.

Ziegler, N. P., Webb, N. P., Chappell, A., and LeGrand, S. L.: Scale invariance of albedo-based wind friction velocity, J. Geophys. Res.-Atmos., 125, e2019JD031978, https://doi.org/10.1029/2019JD031978, 2020.

895   Zobeck, T. M., Sterk, G., Funk, R., Rajot, J. L., Stout, J. E., and Van Pelt, R. S.: Measurement and data analysis methods for field-scale wind erosion studies and model validation, Earth Surf. Proc. Land., 28, 1163–1188, https://doi.org/10.1002/esp.1033, 2003.
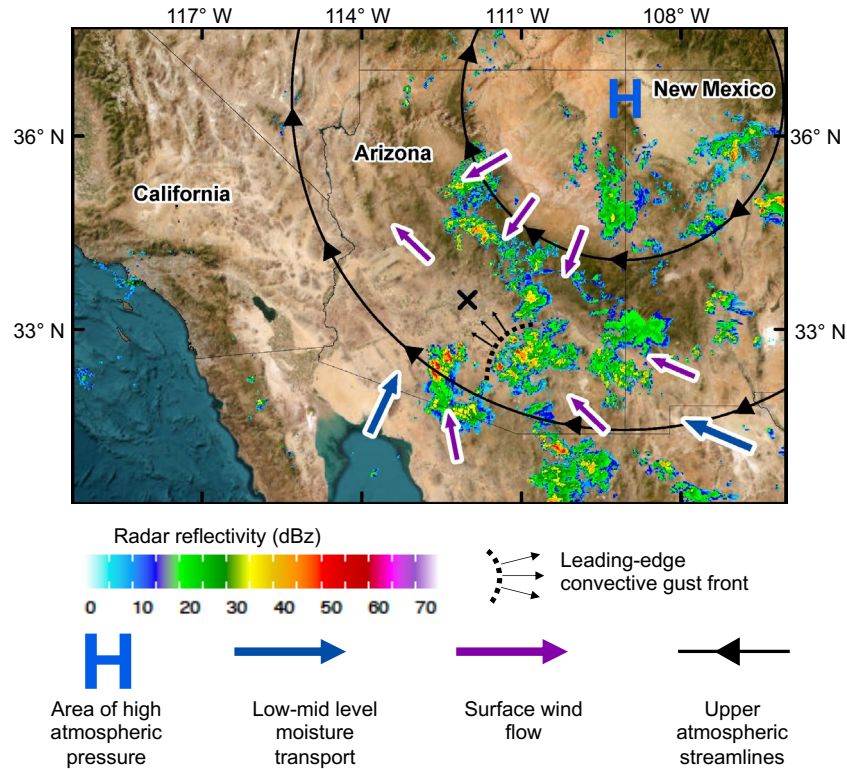
Figure 1. A summary overview of the atmospheric forcing conditions associated with a convective dust storm that occurred 3-4 July 2014. The event was characterized by a persistent broad high pressure (blue H), clockwise upper-air circulation (black streamlines and arrows), mid- to low-level moisture transport (blue arrows) from the Gulf of California and the Gulf of Mexico, and surface wind vectors (purple arrows) converging downslope of the Mogollon Rim. These conditions initiated and sustained several convective systems that merged near and around Phoenix, Arizona (denoted with a black ×). The shaded overlay shows the national radar reflectivity composite imagery at the storm's peak intensity on 4 July 2014, 0100 UTC. Shortly after, the gust front at the leading edge of the convective cell south of Phoenix (dashed black line) moved northwest (storm motion denoted by thin black arrows) over the greater Phoenix area. A wall of thick dust associated with the storm lofted and transported along the gust front.
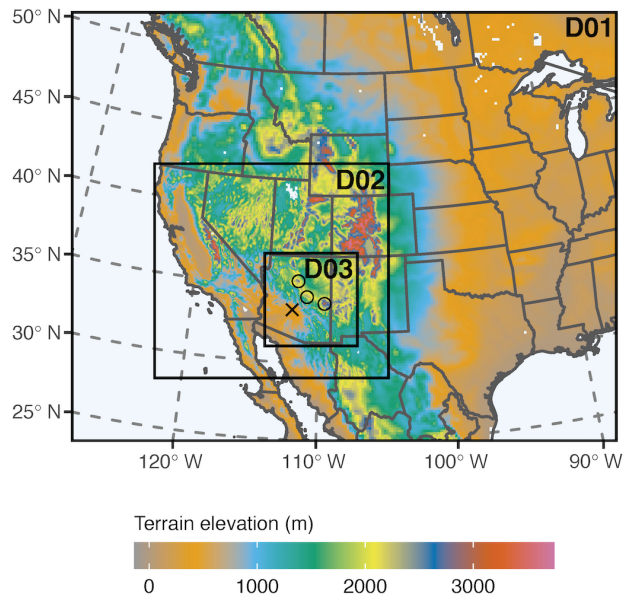
Figure 2. Telescoping model domains with shading showing terrain elevation in meters. The black × marks the location of Phoenix, Arizona. The elevated terrain feature northeast of Phoenix marked by a line of hollow circles is the Mogollon Rim.
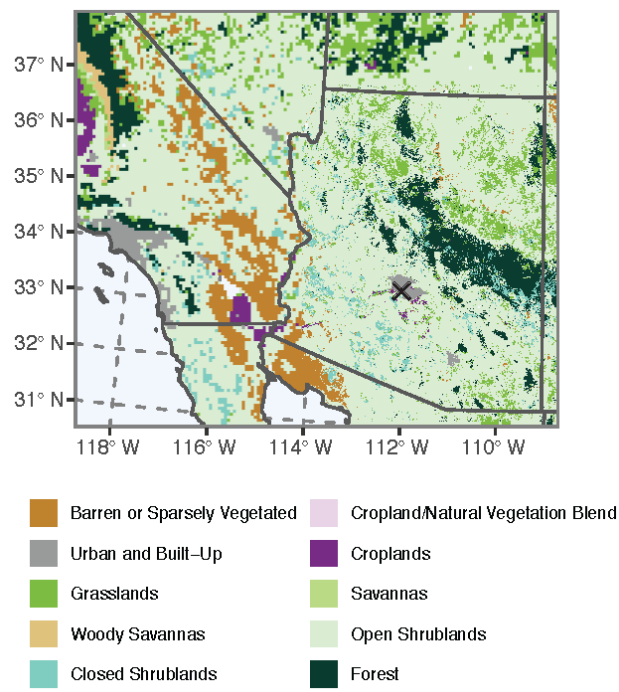
Figure 3. Prescribed land use categories assumed for the model domain. The black × marks the location of Phoenix, Arizona.
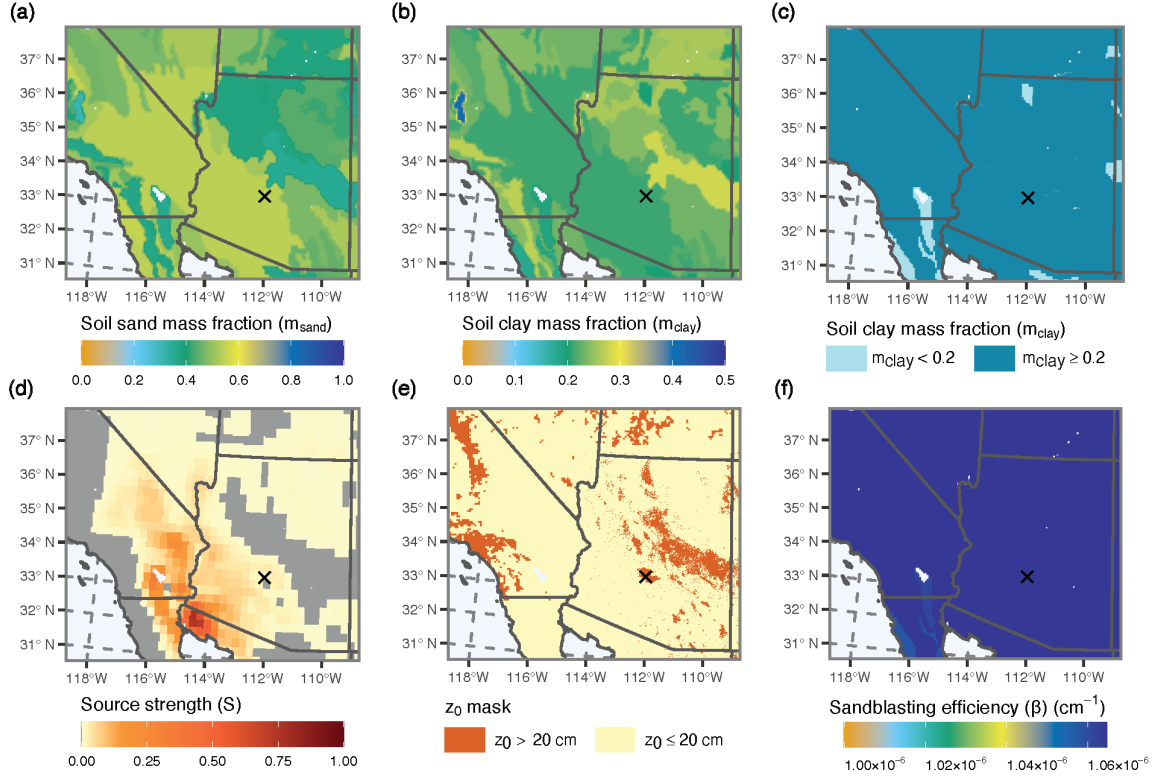
Figure 4. Important terrain attribute features considered in the AFWA dust emission flux calculation, including (a) soil sand mass fraction, (b) soil clay mass fraction (m_{clay}), (c) the clay mass fraction threshold affecting dust emission, (d) dust source strength (S; grey areas are masked), (e) the threshold aerodynamic roughness length (z_0) required for dust emission, and (f) sandblasting efficiency (β). Note that β (panel f) is relatively homogenous due to the clay-rich soil content of the domain and is capped at 1.06×10^{-6} cm^{-1} where the soil composition exceeds 20% clay content. The black $\times$ marks the location of Phoenix, Arizona.
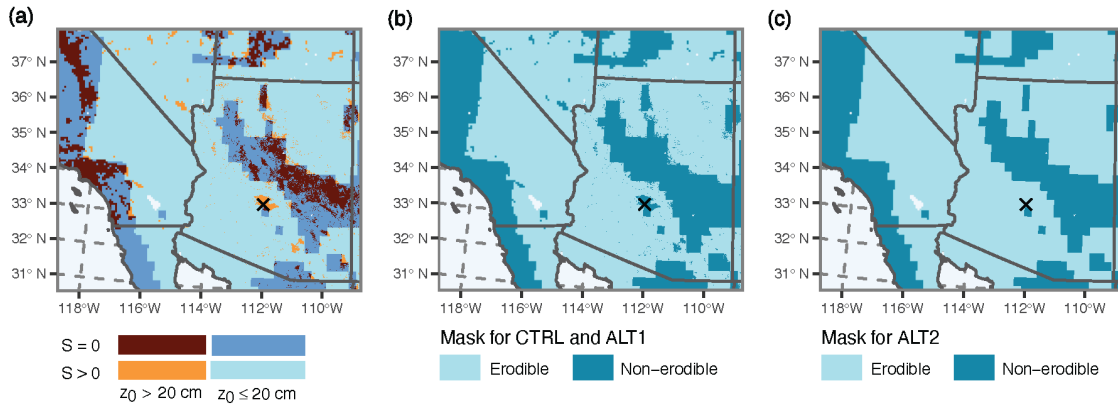
Figure 5. Erodible and non-erodible areas associated with the prescribed roughness and S parameter masks. Erodible area masks in the plot on the left (a) largely overlap, where maroon indicates regions masked by both the z_0 conditional and S parameter, the darker blue represents the area masked by only the S parameter, and orange implies the masking is isolated to the z_0 conditional. Light blue regions in (a) have no masking. The middle plot (b) shows the combined z_0 and S parameter masks applied in the CTRL and ALT1 configurations, and plot (c) shows the S parameter mask applied in ALT2. No masks are applied in the ALT3 or ALT4 configurations. The black $\times$ marks the location of Phoenix, Arizona.
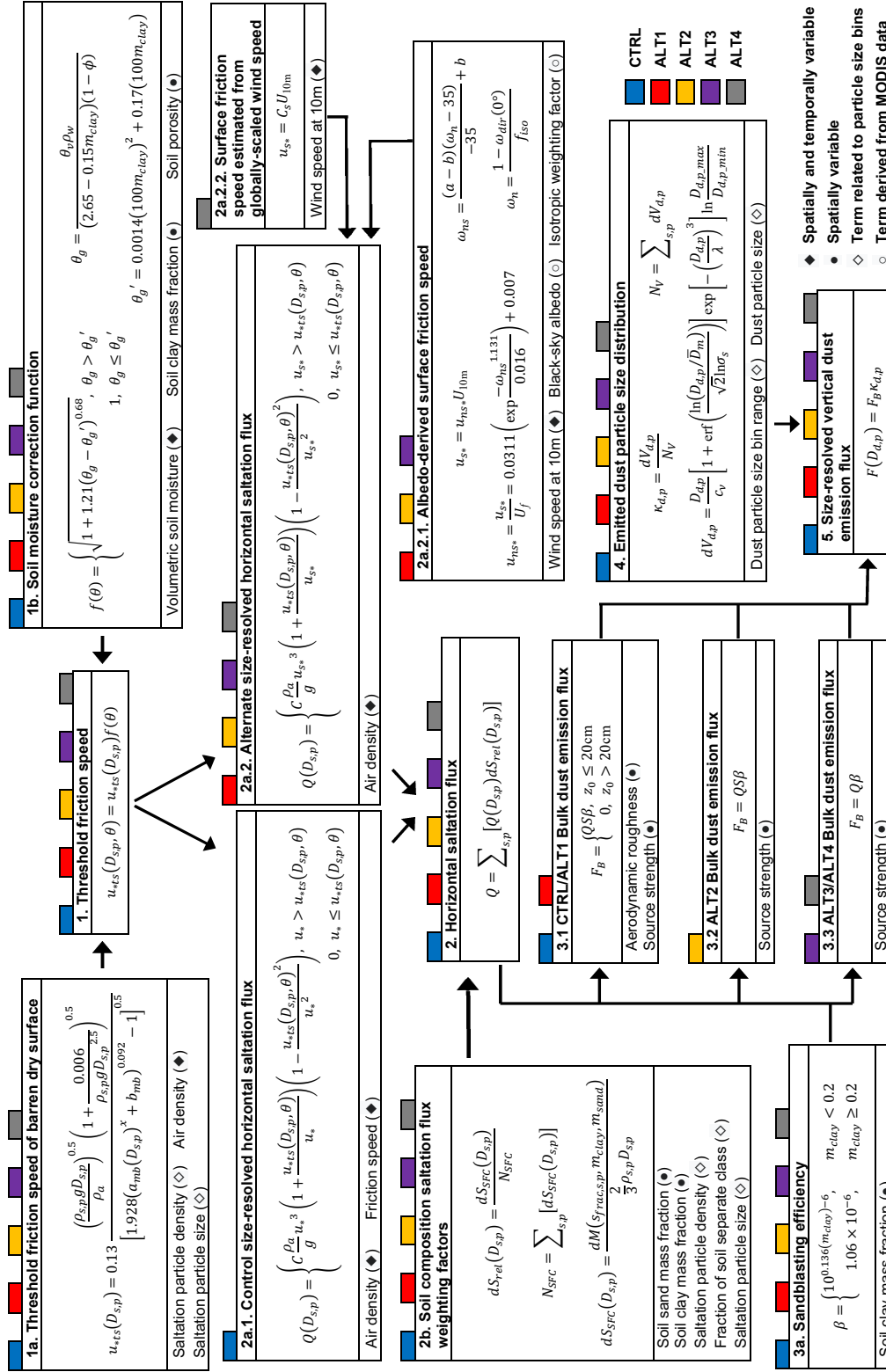
Figure 6. Schematic of the original and modified components of the dust emission module and their required inputs. A black diamond indicates the parameter varies spatially and temporally. A black circle indicates the parameter varies spatially but not temporally, and a hollow diamond means the term is related to a particle size bin attribute table. The hollow circle indicates the field is derived from MODIS data. These input parameters are provided to the AFWA dust emission module by the WRF-Chem model. Color boxes imply which module components are used in the five different test configurations. See the comprehensive variable list in Tables A1-A3 for variable definitions.
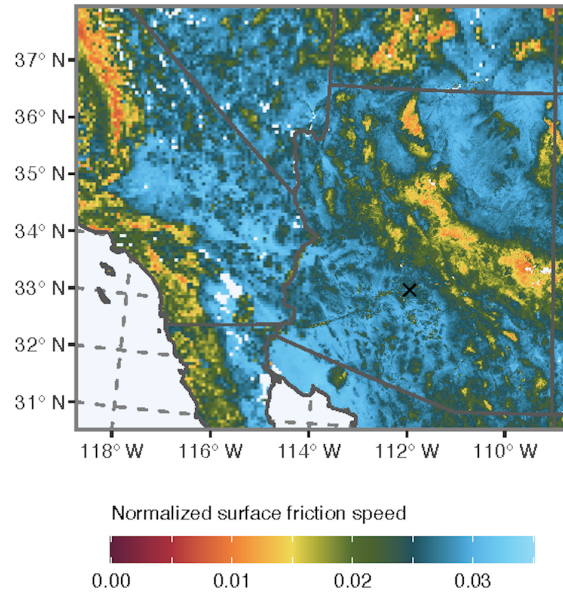
Figure 7. Normalized surface friction speed (u_{ns*}) diagnosed from MODIS data. Due to the relatively short duration of our case study event, the u_{ns*} field remains fixed throughout the simulation. The black × marks the location of Phoenix, Arizona.
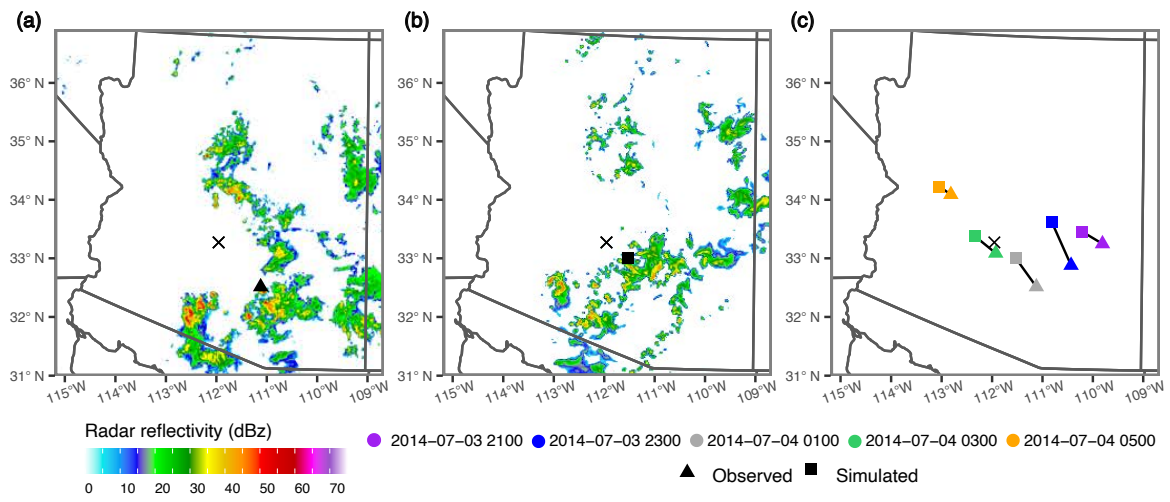
Figure 8. Observed and simulated radar reflectivity for 4 July 2014, 0100 UTC, including an (a) observed composite radar image and (b) the model-simulated radar image. The black × marks the location of Phoenix, Arizona. Triangle and square markers indicate the location of a central point along the leading edge of the convective cell that affected Phoenix in the observed and simulated storms, respectively. The plot on the right (c) shows how these leading edge central point locations evolved over time. Marker colors denote time in UTC.
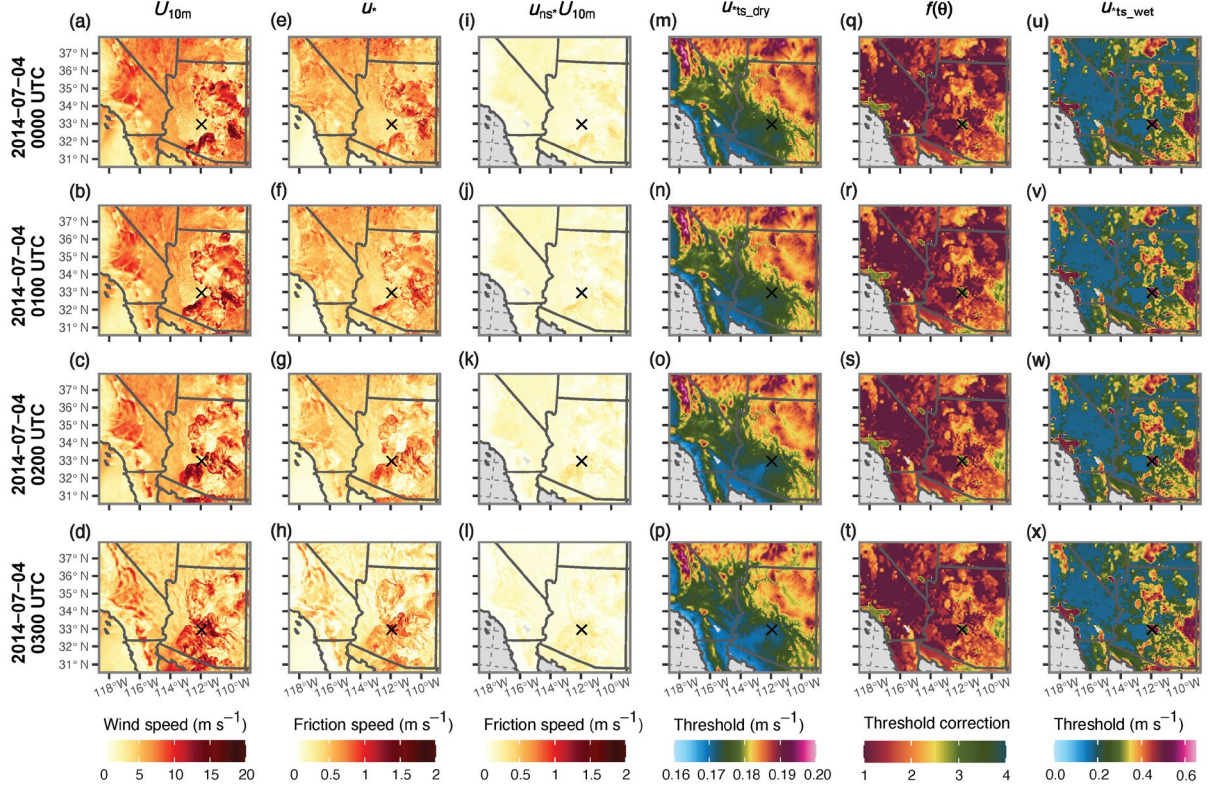
Figure 9. Times series of simulated (a)-(d) 10 m wind speed (U_{10m}; m s^{-1}), (e)-(h) total wind friction speed (u_*; m s^{-1}), (i)-(l) surface friction speed determined from the albedo-based drag parameterization (u_{s*}; m s^{-1}), (m)-(p) threshold friction speed for a 69 μm diameter particle for an idealized smooth, dry, and barren soil surface ($u_{*ts}(D_{s,p} = 69 \ \mu$m); m s^{-1}), (q)-(t) the soil moisture-based correction function ($f(\theta)$; dimensionless), (u)-(x) and soil wetness-corrected threshold friction speed for a 69 μm diameter particle ($u_{*ts}(D_{s,p} = 69 \ \mu$m, θ); m s^{-1}) from 0000 to 0300 UTC on 4 July 2014. The u_{*ts_dry} and u_{*ts_wet} symbols used in the figure labeling represent $u_{*ts}(D_{s,p} = 69 \ \mu$m) and ($u_{*ts}(D_{s,p} = 69 \ \mu$m, θ), respectively. The wetness-corrected threshold is the product of the threshold friction speed and the soil moisture-based correction function. Note the differences in color bar scaling. The black × marks the location of Phoenix, Arizona.
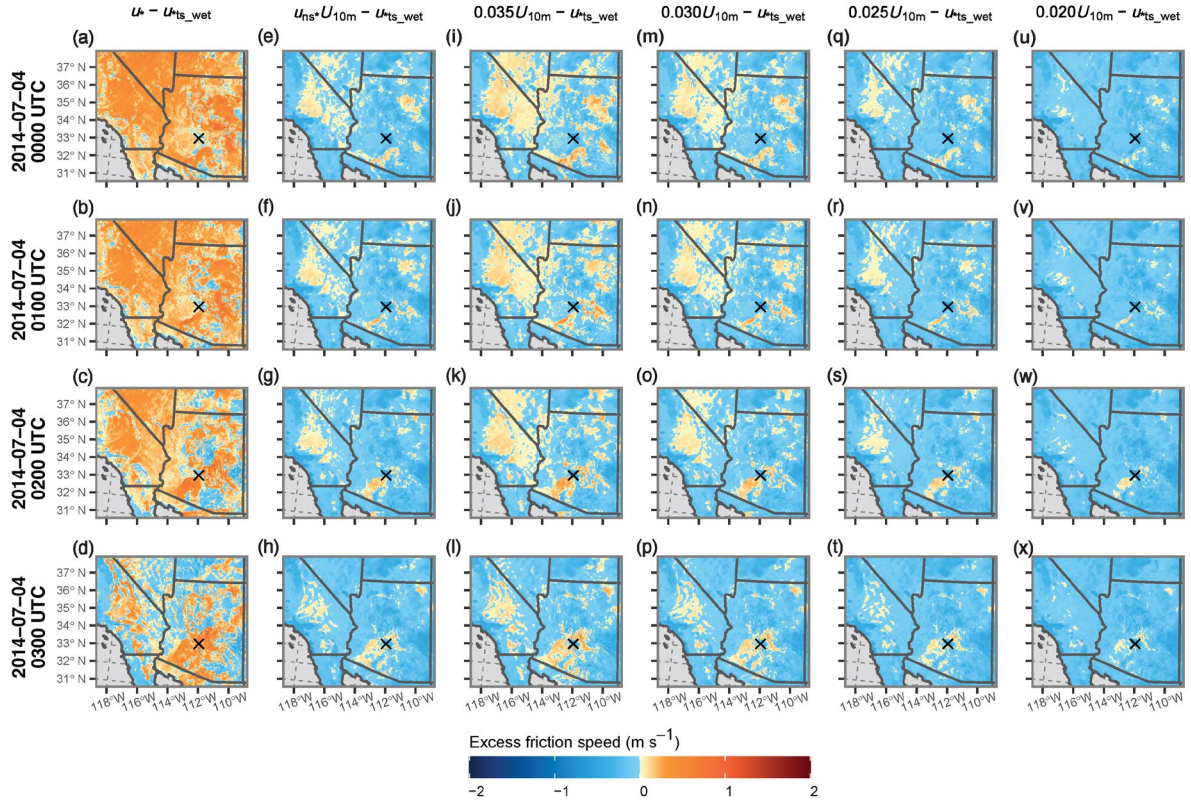
Figure 10. Times series of excess friction speed (u_{*ex}; m s^{-1}) calculated by subtracting the moisture-corrected threshold friction speed for a 69 μm diameter particle, $u_{*ts}(D_{s,p} = 69\ \mu\text{m}, \theta)$, from the wind forcing parameter driving dust production from 0000 to 0300 UTC on 4 July 2014. The u_{*ts_wet} symbol used in the figure labeling represents $u_{*ts}(D_{s,p} = 69\ \mu\text{m}, \theta)$. Plots provided include (a)-(d) u_{*ex} calculated using total friction speed, (e)-(h) surface friction speed determined from the albedo-based drag parameterization, and (i)-(x) four instances of 10 m wind speeds scaled using a global tuning constant as the wind forcing parameter. The black $\times$ marks the location of Phoenix, Arizona.

Figure 11. Times series of horizontal saltation flux (Q; μg m^{-1} s^{-1}) for each test configuration (CTRL, ALT1, ALT2, ALT3, and ALT4) with non-erodible area masking applied from 0000 to 0300 UTC on 4 July 2014. The black $\times$ marks the location of Phoenix, Arizona.
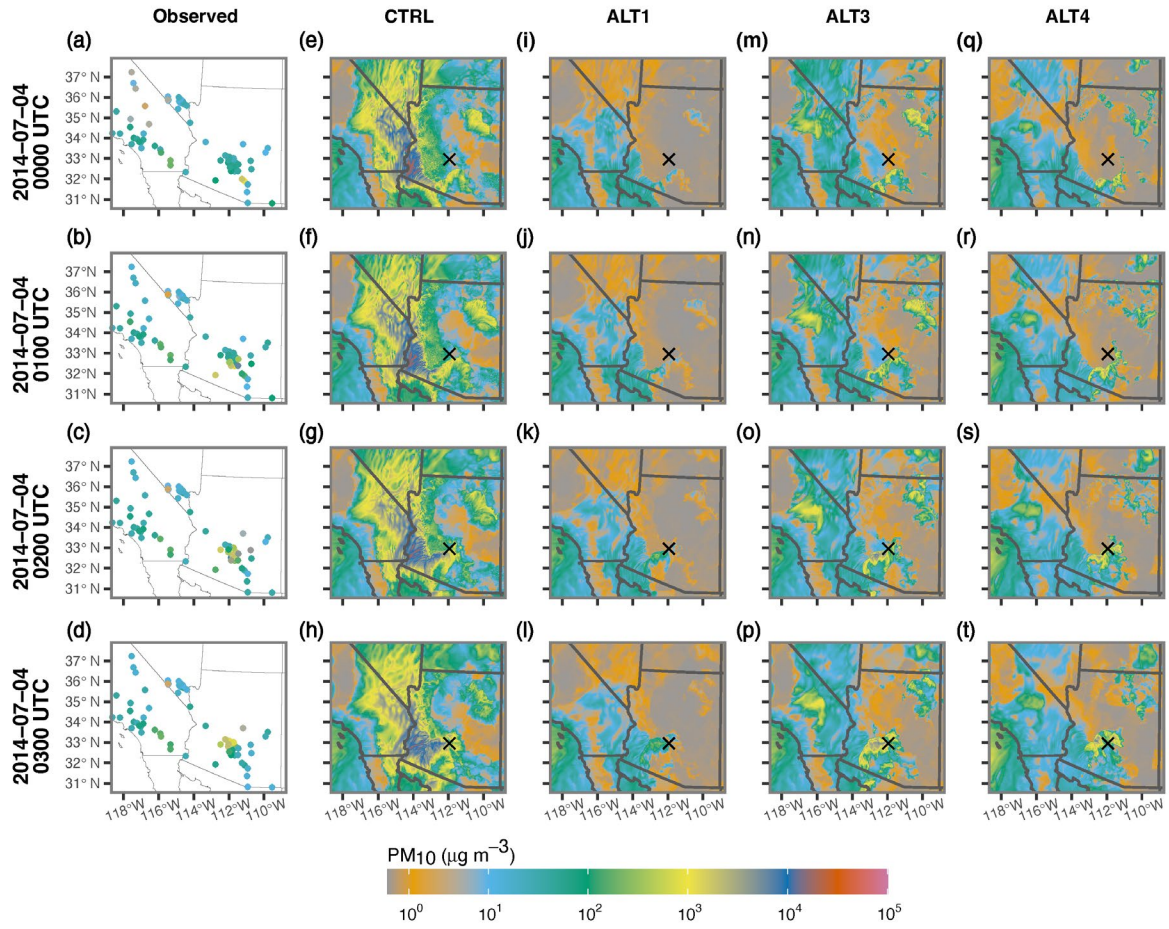
Figure 12. Times series of observed and simulated PM$_{10}$ concentration for each test configuration (CTRL, ALT1, ALT3, and ALT4) in μg m-3 from 0000 to 0300 UTC on 4 July 2014. The black $\times$ marks the location of Phoenix, Arizona. The ALT2 configuration results are not included in this figure since they are nearly identical to results from the ALT1 configuration.
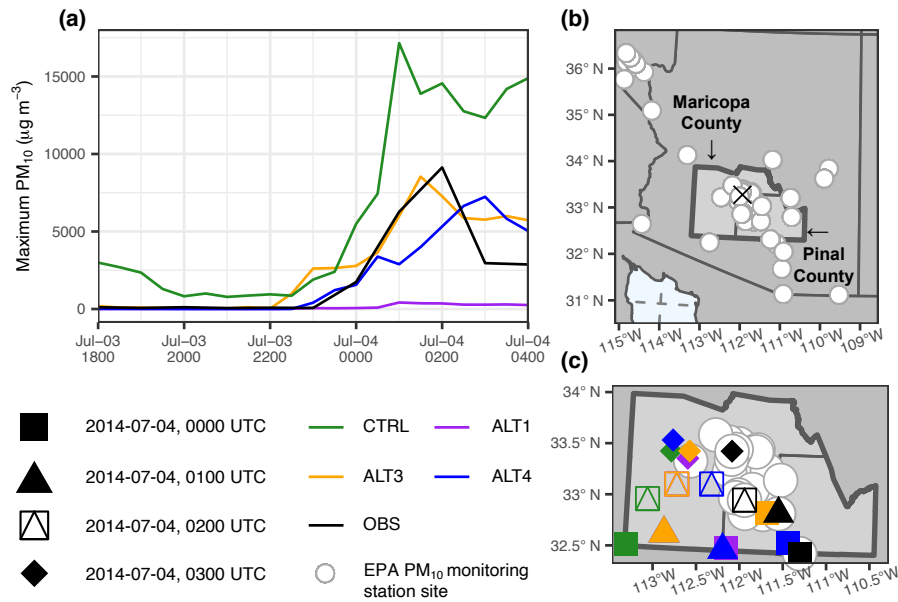
Figure 13. (a) Time series of observed (OBS) and simulated (CTRL, ALT1, ALT3, and ALT4) maximum PM_{10} concentration in μg m^{-3} for the combined Maricopa and Pinal counties in Arizona. Plot (b) highlights how most EPA monitoring stations in Arizona are in Maricopa County and Pinal County, clustered around the Phoenix metropolitan area (marked by the black ×). We used the hourly maximum PM_{10} concentrations from the combined Maricopa and Pinal county areas for our assessment due to the shifted nature of the main dust-producing outflow boundary recorded by the EPA stations situated around Phoenix, Arizona in the simulations. The map zoom in (c) of the Maricopa County and Pinal County boundaries shows the EPA station locations relative to the hourly PM10 maximum values sampled for each test configuration and the observations between 4 July 2014, 0000-0300 UTC. The ALT2 configuration results are not included in this figure since they are nearly identical to results from the ALT1 configuration. Note the CTRL, ALT1, and ALT3 PM_{10} maximum value sites overlap at 2014-07-04, 0100 UTC, and the ALT1 and ALT3 sites are co-located at 2014-07-04, 0200 UTC.
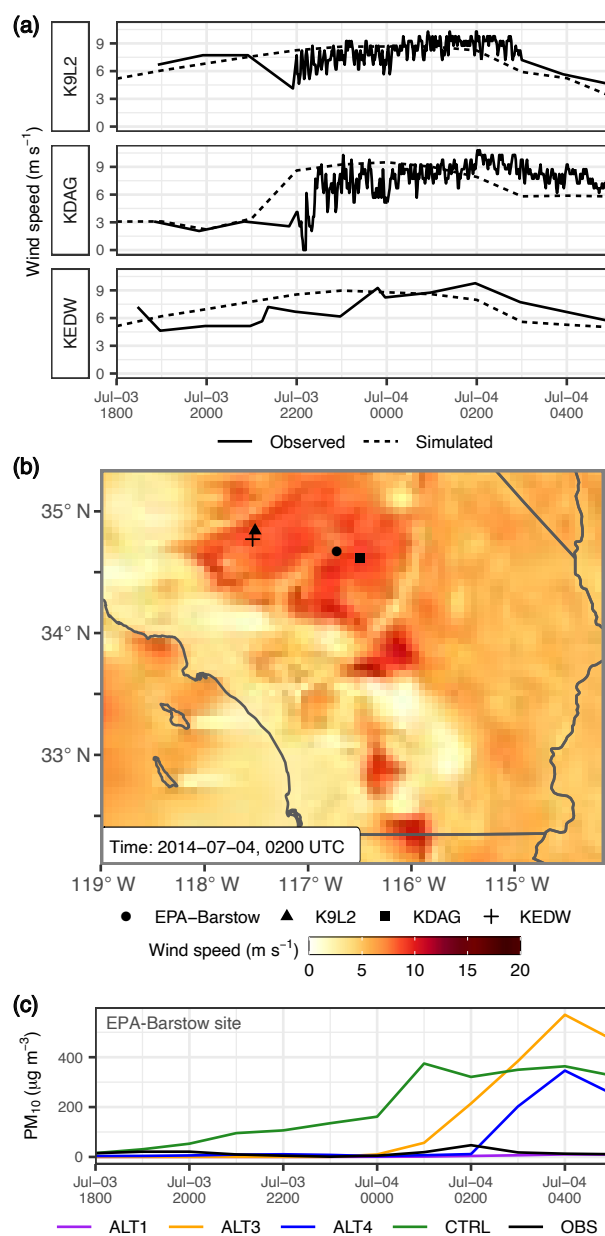
Figure 14. Simulated and observed (a) surface wind speed and (c) PM$_{10}$ values for ASOS and EPA station locations in the Mojave Desert area associated with the erroneously simulated PM$_{10}$ plume. The spatial plot (b) shows the station locations relative to the area of maximum wind speed simulated by the model over the Mojave Desert at 4 July 2014, 0200 UTC, when observed PM$_{10}$. values for the general location peaked.
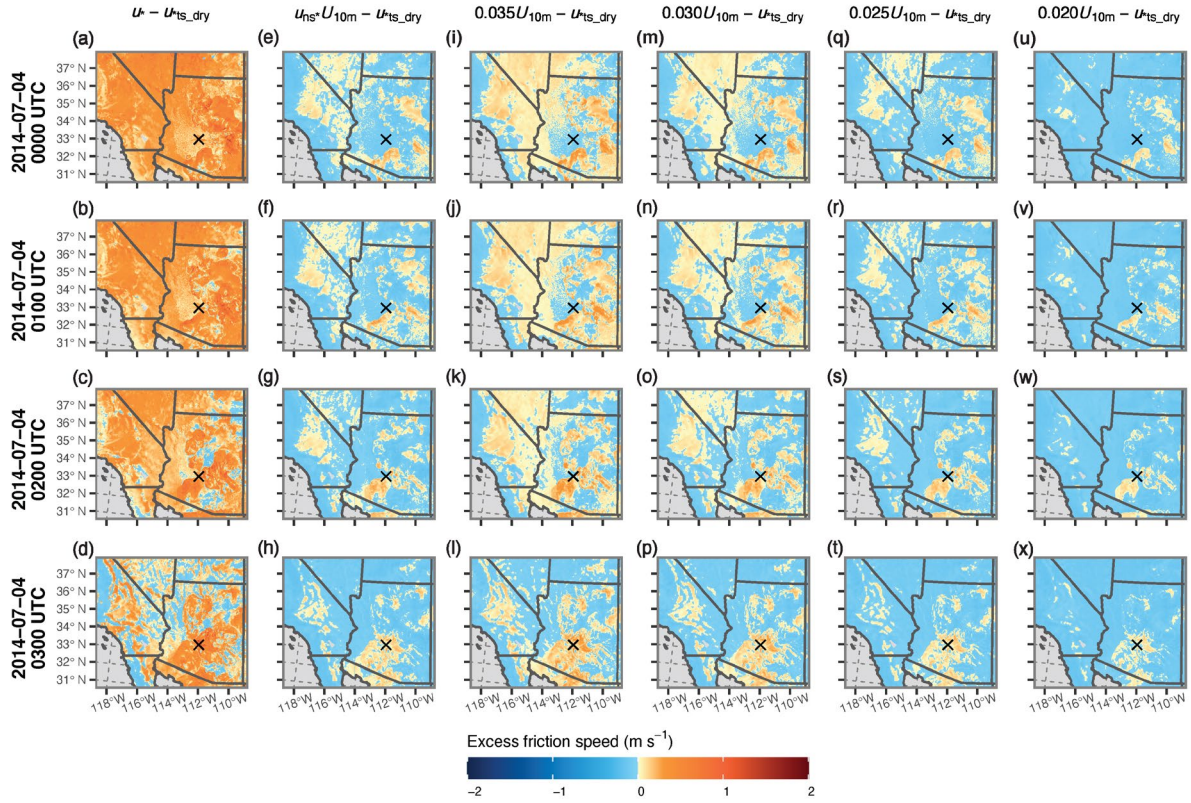
Figure 15. Times series of excess friction speed (u_{*ex}; m s^{-1}) calculated by subtracting the moisture-corrected threshold friction speed for a 69 μm diameter particle, $u_{*ts}(D_{s,p} = 69\ \mu\text{m}, \theta)$, from the wind forcing parameter driving dust production from 0000 to 0300 UTC on 4 July 2014. The u_{*ts_wet} symbol used in the figure labeling represents $u_{*ts}(D_{s,p} = 69\ \mu\text{m}, \theta)$. Plots provided include (a)-(d) u_{*ex} calculated using total friction speed, (e)-(h) surface friction speed determined from the albedo-based drag parameterization, and (i)-(x) four instances of 10 m wind speeds scaled using a global tuning constant as the wind forcing parameter. The black $\times$ marks the location of Phoenix, Arizona. Excess friction speed (u_{*ex_dry}; m s^{-1}) calculated by subtracting the dry threshold friction speed for a 69 μm diameter particle, $u_{*ts}(D_{s,p} = 69\ \mu\text{m})$, from the wind forcing parameter driving dust production from 0000 to 0300 UTC on 4 July 2014. The u_{*ex_dry} symbol used in the figure labeling represents $u_{*ts}(D_{s,p} = 69\ \mu\text{m})$. Plots provided include (a)-(d) excess friction speed calculated using total friction speed, (e)-(h) surface friction speed determined from the albedo-based drag parameterization, and (i)-(x) four instances of 10 m wind speeds scaled using a global tuning constant as the wind forcing parameter. The black $\times$ marks the location of Phoenix, Arizona.
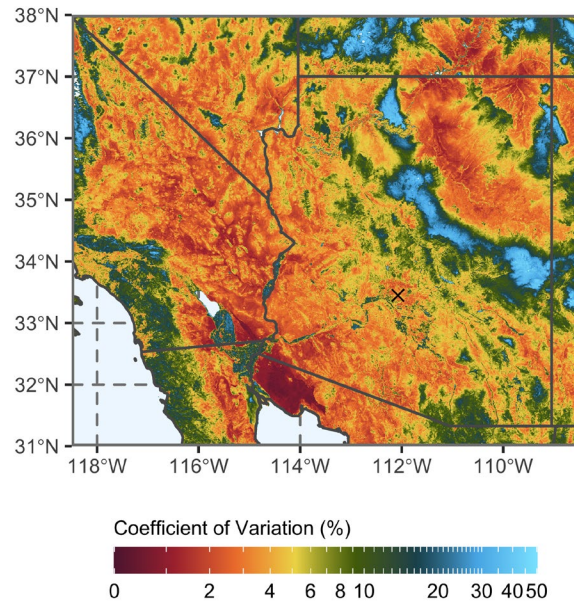
Figure 16. The spatiotemporal variability of u_{ns*} for the 2001-2021 MODIS record shown as the coefficient of variation of monthly u_{ns*} as a percentage. The black $\times$ marks the location of Phoenix, Arizona. Note the colorbar tick marks increase in increments of 5% after the 30% mark.

Table 1. Saltation particle size bins and their associated effective diameters (adapted from LeGrand et al., 2019, Table 1). Particle diameters are presented here in micrometers but handled in units of centimeters within the model.

Saltation size bin	Effective diameter ($D_{s,p}$) (μm)
1	1.42
2	2.74
3	5.26
4	10
5	19
6	36.2
7	69
8	131
9	250

Table 2. Dust particle size bins and their associated attributes (adapted from LeGrand et al., 2019, Table 2). Particle diameters are presented here in micrometers but handled in units of centimeters within the model.

Dust size bin	Effective diameter ($D_{d,p}$) (μm)	Distribution fraction ($\kappa_{d,p}$)
1	1.46	0.1074
2	2.8	0.1012
3	4.8	0.2078
4	9	0.4817
5	16	0.1019

Table 3. WRF-Chem physics and chemistry parameterizations. Note, the option numbers may be different in later model versions.

Parameterization	Scheme	Namelist variable	Option
Cumulus (D01 & D02 only)	NSAS (Han and Pan, 2011)	cu_physics	14
Surface model	Noah (Ek et al., 2003)	sf_surface_physics	2
Surface layer	MYNN (Nakanishi and Niino, 2004)	sf_sfclay_physics	5
Boundary layer	MYNN 2.5 (Nakanishi and Niino, 2004)	bl_pbl_phsyics	5
Radiation (shortwave & longwave)	RRTMG (Iacono et al., 2008)	ra_sw(lw)_physics	4
Microphysics	Thompson (Thompson et al., 2008)	mp_physics	8
Chemistry	GOCART simple no ozone chemistry	chem_opt	301
Dust emission	AFWA (LeGrand et al., 2019)	dust_opt	3
Background emissions	GOCART simple	emiss_opt	5
Aerosol radiative feedbacks	Off	aer_ra_feedback	0
Aerosol optics	Maxwell approximation	aer_op_opt	2

Table 4. Size-resolved saltation and bulk vertical dust flux treatments associated with each test case.

Test	Size-resolved saltation treatment $Q(D_{s,p})$	u_{s*} equation	Bulk vertical dust flux treatment (F_B)
CTRL	$\begin{cases} C\frac{\rho_a}{g}u_*^3\left(1+\frac{u_{*ts}(D_{s,p},\theta)}{u_*}\right)\left(1-\frac{u_{*ts}(D_{s,p},\theta)^2}{u_*^2}\right), & u_* > u_{*ts}(D_{s,p},\theta) \\ 0, & u_* \leq u_{*ts}(D_{s,p},\theta) \end{cases}$		$\begin{cases} QS\beta, & z_0 \leq 20\text{ cm} \\ 0, & z_0 > 20\text{ cm} \end{cases}$
ALT1	$\begin{cases} C\frac{\rho_a}{g}u_{s*}^3\left(1+\frac{u_{*ts}(D_{s,p},\theta)}{u_{s*}}\right)\left(1-\frac{u_{*ts}(D_{s,p},\theta)^2}{u_{s*}^2}\right), & u_{s*} > u_{*ts}(D_{s,p},\theta) \\ 0, & u_{s*} \leq u_{*ts}(D_{s,p},\theta) \end{cases}$	$u_{ns*}U_{10\text{m}}$	$\begin{cases} QS\beta, & z_0 \leq 20\text{ cm} \\ 0, & z_0 > 20\text{ cm} \end{cases}$
ALT2	$\begin{cases} C\frac{\rho_a}{g}u_{s*}^3\left(1+\frac{u_{*ts}(D_{s,p},\theta)}{u_{s*}}\right)\left(1-\frac{u_{*ts}(D_{s,p},\theta)^2}{u_{s*}^2}\right), & u_{s*} > u_{*ts}(D_{s,p},\theta) \\ 0, & u_{s*} \leq u_{*ts}(D_{s,p},\theta) \end{cases}$	$u_{ns*}U_{10\text{m}}$	$QS\beta$
ALT3	$\begin{cases} C\frac{\rho_a}{g}u_{s*}^3\left(1+\frac{u_{*ts}(D_{s,p},\theta)}{u_{s*}}\right)\left(1-\frac{u_{*ts}(D_{s,p},\theta)^2}{u_{s*}^2}\right), & u_{s*} > u_{*ts}(D_{s,p},\theta) \\ 0, & u_{s*} \leq u_{*ts}(D_{s,p},\theta) \end{cases}$	$u_{ns*}U_{10\text{m}}$	$Q\beta$
ALT4	$\begin{cases} C\frac{\rho_a}{g}u_{s*}^3\left(1+\frac{u_{*ts}(D_{s,p},\theta)}{u_{s*}}\right)\left(1-\frac{u_{*ts}(D_{s,p},\theta)^2}{u_{s*}^2}\right), & u_{s*} > u_{*ts}(D_{s,p},\theta) \\ 0, & u_{s*} \leq u_{*ts}(D_{s,p},\theta) \end{cases}$	$C_s U_{10\text{m}}$	$Q\beta$

Table A1. Variable list. Units are provided in terms of mass [M], length [L], and Time [T]. In the Type column, "C" implies the parameter is a prescribed constant or global scaling factor, "V" indicates the parameter is a prescribed 1-dimensional array of size bin-related settings, "SV" parameters are spatially varying static fields, and "STV" parameters are spatiotemporally varying dynamic fields.

Variable	Name (Value)	Units	Type
a	Dimensionless scaling parameter (0.0001)	Unitless	C
a_{mb}	Dimensional constant (1331 cm^{-x})	L^{-x}	C
b	Dimensionless scaling parameter (0.1)	Unitless	C
b_{mb}	Dimensionless constant (0.38)	Unitless	C
C	Dimensionless constant (1.0)	Unitless	C
C_s	10 m wind speed global scaling factor (Set by model user)	Unitless	C
c_v	Dimensional constant (12.62×10^{-4} cm)	L	C
$D_{d,p}$	Particle diameter of dust size bin p	L	V
D_{d,p_max}	Maximum particle diameter of dust size bin p	L	V
D_{d,p_min}	Minimum particle diameter of dust size bin p	L	V
$\bar{D}_m$	Emitted dust particle mass median diameter (3.4×10^{-4} cm)	L	C
$D_{s,p}$	Particle diameter of saltation size bin p	L	V
$d\_\_$	Distributions of particle property $\_\_$		SV or STV
$dM(s_{\mathrm{frac},s,p}, m_{\mathrm{clay}}, m_{\mathrm{sand}})$	Particle mass distribution fraction for saltation size bin p	Unitless	SV
$dS_{\mathrm{SFC}}(D_{s,p})$	Basal surface coverage fraction for saltation size bin p	L^{2}M^{-1}	SV
$dS_{\mathrm{rel}}(D_{s,p})$	Relative weighting factor for saltation size bin p	Unitless	SV
$dV_{d,p}$	Normalized volume distribution for dust size bin p	Unitless	SV
F_B	Bulk dust emission flux	ML^{-2}T^{-1}	STV
$F(D_{d,p})$	Dust emission flux for dust size bin p	ML^{-2}T^{-1}	STV
$f(\theta)$	Wind friction speed threshold moisture correction function	Unitless	STV
f_{iso}	BRDF isotropic weighting parameter	Unitless	STV
g	Gravitational acceleration constant (981 cm s^{-2})	LT^{-2}	C
m_{clay}	Soil clay mass fraction	Unitless	SV
m_{sand}	Soil sand mass fraction	Unitless	SV
N_{SFC}	Total basal surface area of soil bed	L^{2}M^{-1}	SV
N_V	Total normalized emitted dust volume	Unitless	V
Q	Horizontal saltation flux	ML^{-1}T^{-1}	STV
$Q(D_{s,p})$	Horizontal saltation flux for saltation size bin p	ML^{-1}T^{-1}	STV
S	Dust source strength function	Unitless	SV
$s_{\mathrm{frac},s,p}$	Soil separate class mass fraction for saltation size bin p	Unitless	V
$U_{10\mathrm{m}}$	Wind speed at 10 m above ground level	LT^{-1}	STV
U_f	Freestream wind speed	LT^{-1}	STV
u_*	Wind friction speed	LT^{-1}	STV

Table A2. Variable list continued. Units are provided in terms of mass [M], length [L], and Time [T]. In the Type column, "C" implies the parameter is a prescribed constant or global scaling factor, "V" indicates the parameter is a 1-dimensional array of size bin-related settings, "SV" parameters are spatially varying static fields, and "STV" parameters are spatiotemporally varying dynamic fields.

Variable	Name (Value)	Units	Type
u_{*ex}	Excess friction speed	LT^{-1}	STV
u_{*ex_dry}	Excess friction speed assuming air-dry soil conditions	LT^{-1}	STV
$u_{*ts}(D_{s,p})$	Idealized smooth surface wind friction speed threshold required to mobilize particles associated with saltation size bin p	LT^{-1}	STV
$u_{*ts}(D_{s,p},\theta)$	Idealized smooth surface wind friction speed threshold required to mobilize particles associated with saltation size bin p corrected for soil moisture	LT^{-1}	STV
u_{ns*}	Soil surface component of wind friction speed normalized by the freestream wind speed	Unitless	STV
u_{r*}	Roughness component of wind friction speed	LT^{-1}	STV
u_{s*}	Soil surface component of wind friction speed	LT^{-1}	STV
x	Dimensionless constant (1.56)		
z_0	Aerodynamic roughness length	L	STV
z_i	Terrain elevation above sea level of grid cell i	L	SV
$z_{\max}$	Maximum terrain elevation above sea level in a $10° \times 10°$ area	L	SV
$z_{\min}$	Minimum terrain elevation above sea level in a $10° \times 10°$ area	L	SV
β	Sandblasting efficiency factor	L^{-1}	SV
θ	Soil moisture		STV
θ_g	Gravimetric soil moisture	MM^{-1}	STV
$\theta_{g'}$	Gravimetric soil moisture without effect on capillary forces	MM^{-1}	SV
θ_v	Volumetric soil moisture	L^3L^{-3}	STV
$\kappa_{d,p}$	Size distribution weighting factor for dust size bin p	Unitless	V
λ	Crack propagation length (12.0×10^{-4} cm)	L	C
ρ_a	Air density	ML^{-3}	STV
$\rho_{s,p}$	Particle density of saltation size bin p	ML^{-3}	V
ρ_w	Water density (1.0 g cm^{-3})	ML^{-3}	C
σ_s	Geometric standard deviation (3.0)	Unitless	C
τ	Wind shear stress	$ML^{-1}T^{-2}$	STV
τ_{r*}	Roughness component of wind shear stress	$ML^{-1}T^{-2}$	STV
τ_{s*}	Soil surface component of wind shear stress	$ML^{-1}T^{-2}$	STV

Table A3. Variable list continued. Units are provided in terms of mass [M], length [L], and Time [T]. In the Type column, "C" implies the parameter is a prescribed constant or global scaling factor, "V" indicates the parameter is a 1-dimensional array of size bin-related settings, "SV" parameters are spatially varying static fields, and "STV" parameters are spatiotemporally varying dynamic fields.

Variable	Name (Value)	Units	Type
ϕ	Soil porosity	L^3L^{-3}	SV
ω	Albedo	Unitless	STV
$\omega_{\mathrm{dir}}(0°)$	Black-sky albedo at nadir	Unitless	STV
ω_n	Normalized albedo used to represent the normalized proportion of shadow	Unitless	STV
ω_{ns}	Empirically-scaled albedo used to represent the empirically-scaled proportion of shadow	Unitless	STV